12/11/1996 SD

ANL/ESD/TM-135

Application of Oxygen-Enriched Combustion for Locomotive Diesel Engines, Phase I

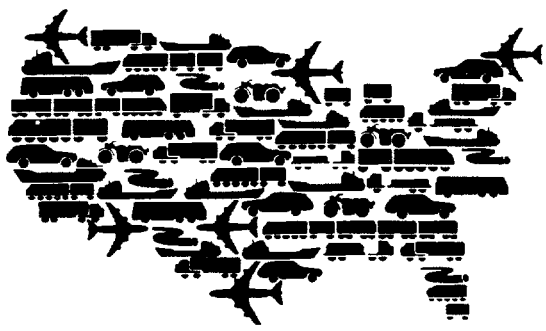

Center for Transportation Research

Argonne National Laboratory

Operated by The University of Chicago,
under Contract W-31-109-Eng-38, for the

United States Department of Energy

Argonne National Laboratory

Argonne National Laboratory, with facilities in the states of Illinois and Idaho, is owned by the United States Government, and operated by the University of Chicago under the provisions of a contract with the Department of Energy.

This technical memo is a product of Argonne's Energy Systems (ES) Division. For information on the division's scientific and engineering activities, contact:

Director, Energy Systems Division
Argonne National Laboratory
Argonne, Illinois 60439-4815
Telephone (630) 252-3724

Presented in this technical memo are preliminary results of ongoing work or work that is more limited in scope and depth than that described in formal reports issued by the ES Division.

Publishing support services were provided by Argonne's Information and Publishing Division (for more information, see IPD's home page: http://www.ipd.anl.gov/).

Disclaimer

DISCLAIMER

ANL/ESD/TM-135

Application of Oxygen-Enriched Combustion for Locomotive Diesel Engines, Phase I

by R.B. Poola, R.R. Sekar, and D.N. Assanis*

Center for Transportation Research, Energy Systems Division
Argonne National Laboratory, 9700 South Cass Avenue, Argonne, Illinois 60439

September 1996

Work sponsored by United States Department of Energy,
Office of Energy Research, Laboratory Technology Research,
under a Cooperative Research and Development Agreement
with Association of American Railroads, Washington, D.C.

---

*Assanis is affiliated with the Department of Mechanical Engineering and Applied Mechanics of the University of Michigan, Ann Arbor.

This report is printed on recycled paper.

Contents

ACKNOWLEDGMENTS. vii

ABSTRACT 1

1 INTRODUCTION 3

2 DIESEL ENGINE SIMULATION 5

2.1 Introduction 5
2.2 Basic Assumptions about System Models 5
2.2.1 Reciprocator Engine Model 5
2.2.2 Other Component Models 6
2.3 Modeling of Reciprocator Engine Processes 7
2.3.1 Gas Exchange 7
2.3.2 Ignition Delay Model 8
2.3.3 Combustion Model 9
2.3.4 Turbulent Flow Model 10
2.3.5 Heat Transfer 12
2.3.6 Wall Conduction Model 14
2.3.7 Friction Model 14
2.3.8 NO Emission Model 15
2.4 Other System Component Models 16
2.5 Method of Solution and Program Inputs and Outputs 18
2.5.1 Basic Method of Solution 18
2.5.2 Program Inputs and Outputs 18

3 AIR SEPARATION MEMBRANE 20

3.1 Operating Principle 20
3.2 Membrane Operating Modes 20
3.3 Performance Characteristics 22
3.3.1 Intrinsic Properties 22
3.3.2 Polymer Structure 23
3.3.3 Skin Thickness of Membrane Coating 24
3.3.4 Fiber Dimensions 24
3.3.5 Geometry and Membrane Cartridge Options 24
3.3.6 Flow Patterns 27
3.3.7 Feed Direction 27
3.3.8 Feed Conditions 28
3.3.9 Arrangement of Separators 28
3.4 Model of an Air Separation Membrane 29

4 RESULTS AND DISCUSSION 31

4.1 Engine Configuration 31
4.2 Model Calibration and Validation 31
4.2.1 Model Matching with Watson's Heat-Release Correlation 31
4.2.2 Model Matching with New Heat-Release Correlation 34
4.3 Engine Gross Performance under Various Oxygen-Enrichment Levels 34
4.4 Effects of Fuel Injection Timing with Oxygen Enrichment 37
4.5 NO Emissions 39
4.6 Membrane Size and Power Requirements 42
4.7 Engine Performance with Membrane Supplying Oxygen-Enriched Air 45
4.8 Oxygen Enrichment vs Turbocharging 46

5 ECONOMIC ANALYSIS 50

5.1 Introduction 50
5.2 Oxygen-Enrichment Systems Determination 50
5.3 Budgeting of Capital 52
5.4 Cash Flow Analysis 53
5.5 Results of Economic Analysis 55

6 SUMMARY AND CONCLUSIONS 59

7 REFERENCES 61

APPENDIX: Scope of Work for Phase II 67

A.1 Purpose 67
A.2 Scope of Work 67

Tables

3.1 Membrane Properties and Input Parameters for Two CMS Materials 30

4.1 Specifications for GE Locomotive Diesel Engine 31

4.2 Matching DES with TRANSENG and Experimental Data at Notch 8 32

4.3 Design Estimates of Membrane Size and Power Requirements for Two Different Materials Operating in Mixed Mode to Supply 26% Oxygen in the Intake Air at Full Load 45

5.1 Oxygen-Enrichment System Costs for Two Different Membrane Materials 51

5.2 Capital Costs of Base Engine and Engine Supplied with 26% Oxygen-Enriched Air 52

5.3 Allowable Tax Depreciation per ACRS 54

5.4 Assumptions about Economic Parameters 54

5.5 First-Year Net Cash Savings 55

5.6 Cash-Flow Analysis for CMS-3 Membrane with 26% Oxygen 56

5.7 Cash-Flow Analysis for CMS-7 Membrane with 26% Oxygen 56

5.8 Cash-Flow Analysis for CMS-3 Membrane with 26% Oxygen and with Exhaust Energy Recovery 57

5.9 Cash-Flow Analysis for CMS-7 Membrane with 26% Oxygen and with Exhaust Energy Recovery 57

5.10 Summary of Economic Analysis 58

Figures

2.1 Turbocharged Diesel System Configuration 6

3.1 Basic Membrane Process for Air Separation 20

3.2 Air Separation Membrane Modes of Operation 21

3.3 Turbocharged Diesel System Configuration Using Oxygen-Rich Air Supplied by Air Separation Membrane 22

3.4 Geometries of the Gas Separation Membranes 25

3.5 Elements of Plate-and-Frame Membrane Module 26

3.6 Elements of Spiral-Wound Membrane Module 26

3.7 Typical Hollow-Fiber Membrane Module 26

3.8 Ideal Flow Patterns in a Membrane Gas Separator 27

3.9 Schematic of a Counterflow Hollow-Fiber Membrane Module with Shell-and-Tube Geometry 28

4.1 Diesel Engine Simulation and TRANSENG Heat-Release Profiles at Full Load 33

4.2 Predicted and Measured Cylinder-Pressure Profiles 33

4.3 Validation of Diesel Simulation with Experimental Results 35

4.4 Effects of Intake Air Oxygen Enrichment on Engine Performance at Various Notch Positions 36

4.5 Effects of Fuel Injection Timing on Performance Characteristics 38

4.6 Fuel Injection Timing Map: Brake Power vs Peak Cylinder Pressure at Various Intake Air Oxygen-Enrichment Levels 39

4.7 Overall Combustion and Stoichiometric Core-Flame Temperatures with Intake Air Oxygen Enrichment 40

4.8 Effects of Oxygen and Injection Timing on NO Emissions in Stoichiometric and Overall Combustion Regions 41

4.9 Nitric Oxide Concentrations at Different Intake Air Oxygen-Enrichment Levels 42

4.10 Variation of Permeate Oxygen Concentration with Stage Cut at Various Pressure Ratios for CMS Membrane Materials 43

4.11 Total Isentropic Work Required by Membrane under Three Operating Modes 44

4.12 Minimum Isentropic Work Required by Membrane Modules at Various Oxygen-Enrichment Levels 44

4.13 Potential of Brake Power Enhancement with Oxygen Enrichment at Full Load 46

4.14 Intake Manifold Pressure with High-Boost Turbocharging Corresponding to Various Intake Air Oxygen-Enrichment Levels 47

4.15 Potential of Oxygen Enrichment over Turbocharging with Increased Boost to Enhance Power Output 48

4.16 Turbine-Exit Temperatures for Both High-Boost Turbocharging and Oxygen Enrichment at Constant Oxygen-to-Fuel Ratio 49

Acknowledgments

The authors acknowledge the support of the U.S. Department of Energy, under contract W-31-109-Eng-38. The authors thank G.R. Cataldi, Association of American Railroads, for his enthusiastic support and technical information. The contribution of experimental data by V.O. Markworth, Southwest Research Institute, is gratefully acknowledged. The authors thank Stuart Nemser, Compact Membrane Systems, Inc., for providing membrane properties and design details and Gary Fleming, Cochrane Compressor Company, for providing blower and vacuum-pump cost estimates. The contributions of Dr. Zoran Filipi in simulating the baseline locomotive engine are gratefully acknowledged. Assistance from Anthony Markel and Kevin Stork during preparation of the report is very much appreciated.

Application of Oxygen-Enriched Combustion for Locomotive Diesel Engines, Phase I

by

R.B. Poola, R.R. Sekar, and D.N. Assanis

Abstract

A thermodynamic simulation is used to study the effects of oxygen-enriched intake air on the performance and nitrogen oxide (NO) emissions of a locomotive diesel engine. The parasitic power of the air separation membrane required to supply the oxygen-enriched air is also estimated. For a given constraint on peak cylinder pressure, the gross and net power outputs of an engine operating under different levels of oxygen enrichment are compared with those obtained when a high-boost turbocharged engine is used. A 4% increase in peak cylinder pressure can result in an increase in net engine power of approximately 13% when intake air with an oxygen content of 28% by volume is used and fuel injection timing is retarded by 4 degrees. When the engine is turbocharged to a higher inlet boost, the same increase in peak cylinder pressure improves power by only 4%. If part of the significantly higher exhaust enthalpies available as a result of oxygen enrichment are recovered, the power requirements of the air separator membrane can be met, resulting in substantial net power improvements. Oxygen enrichment, with its attendant higher combustion temperatures, reduces emissions of particulates and visible smoke but increases NO emissions. However, the proposed oxides of nitrogen (NO_x) standards for locomotives are not as stringent as those for truck and car diesel engines. It is anticipated that a combination of retarded fuel injection timing and post-treatment of exhaust gases, such as the use of monatomic nitrogen, will be adequate to meet the locomotive diesel engine NO_x standards. Therefore, exhaust gas after-treatment and heat recovery would be required if the full potential of oxygen enrichment for improving the performance of locomotive diesel engines is to be realized. The economic analysis shows that the application of oxygen-enrichment technology for locomotive diesel engines is economically feasible and provides high returns on investment. The study also indicates the strong influence of membrane parasitic requirements and exhaust energy recovery on economic benefits to be obtained. Membrane size and auxiliary equipment costs are less sensitive in terms of the overall economics. The capital investment has the shortest payback period (1.13 yr, with an internal rate of return of 95.8%) when 26% oxygen-enriched combustion air is used. If a part of the exhaust energy is recovered while using 26% oxygen-enriched combustion air, the payback period is reduced to 0.57 yr and the internal rate of return is increased to 188.4%. To obtain an economic advantage while using a membrane with higher parasitic power requirements, it is necessary to recover a part of the exhaust energy.

1 Introduction

Both railroads and engine manufacturers face a major challenge if they are to meet the standards for emissions of smoke, particulates, unburned hydrocarbons, and oxides of nitrogen (NO_x) set forth in the U.S. Environmental Protection Agency's (EPA's) proposed regulations for locomotive diesel engines. Railroads also face an increasing demand for higher motive power so that payloads in freight locomotives can be increased. Argonne National Laboratory (ANL) and the Association of American Railroads (AAR) initiated a cooperative research and development agreement to study the application of oxygen-enriched intake air as one method to meet the emissions and power challenges.

A number of analytical and experimental studies (e.g., Sekar et al. 1990; Sekar et al. 1991a,b; Marr et al. 1993) have demonstrated the benefits of using oxygen-enriched intake air in diesel engines. Increasing the oxygen content of a reacting fuel-oxidizer mixture leads to faster burn rates and the ability to burn more fuel at the same stoichiometry (oxygen-to-fuel ratio). These effects have the potential to increase the thermal efficiency and specific power output of a diesel engine. The power increase from a given displacement engine can be suitably exploited to increase the number of locomotive cars or freight. In addition, oxygen enrichment can also be considered as a way to reduce the sudden loss in power output when locomotives operate in underground tunnels and at high altitudes.

When oxygen is added to combustion air, emissions of visible smoke, particulates, and unburned hydrocarbons decrease significantly over a wide load range as a result of the more complete combustion (e.g., Iida and Sato 1988). Added oxygen also leads to shorter ignition delays and offers the potential for burning lower grade and nonpetroleum fuels (Iida and Sato 1988; Sekar et al. 1990). However, the increased oxygen content in the combustion air is also expected to increase NO_x emission levels because of the higher combustion temperatures. The anticipated increase in NO_x emissions could be controlled by retarding fuel injection timing and by using other state-of-the-art concepts, such as exhaust post-treatment with monatomic nitrogen and lean-NO_x catalysts. The objective of the present study is to address, in a systematic way, the key technical issues associated with applying oxygen-enrichment technology to locomotive diesel engines. These issues include (1) optimizing the level of oxygen enrichment in the intake air, (2) designing an air separation membrane and assessing its parasitic power requirements, and (3) exploring the merits of injection retard for controlling peak pressure and NO emissions. The economic feasibility of oxygen-enrichment technology for locomotive diesel engines is also examined.

An appropriately modified computer simulation of a turbocharged diesel engine is used to study the effects of oxygen-enriched intake air on the performance and NO emissions of a locomotive diesel engine. The physical and operating characteristics of an air separation membrane are briefly reviewed, and a simplified model is proposed to estimate the module size and parasitic power required to supply the desired oxygen-enrichment level in the intake air. On the basis of engine and membrane models, the net improvements in brake power achieved by an engine equipped with an air separation membrane to supply the oxygen-enriched intake air are

computed. Use of oxygen-enriched air is compared with turbocharging to a higher inlet boost as a means to increase power output. The effects of retarded fuel injection timing are also studied in conjunction with oxygen-enriched intake air. Finally, the potential for enhanced exhaust heat recovery when using oxygen enrichment is assessed. Other aspects of oxygen enrichment, such as a reduction in particulates, smoke, and unburned hydrocarbons and the ability to burn lower-grade fuels, are not the subject of this report but have been studied earlier (e.g., Sekar et al. 1990; Sekar et al. 1991a,b).

An economic analysis is made to evaluate the feasibility and cost benefits of oxygen-enrichment technology for locomotive diesel engines. Three types of capital budget techniques are employed to estimate the payback period and rate of return on capital investments. For the purpose of economic analysis, an oxygen-enrichment level of 26% by volume supplied from two different membranes (operating in a mixed mode) for a 12-cylinder locomotive diesel engine (operating at its full load) is considered. The influence of membrane parasitic power requirements, membrane size, and exhaust energy recovery on economic parameters is studied. The net economic benefits are compared between two membranes supplying 26% oxygen-enriched combustion air, with and without exhaust energy recovery.

2 Diesel Engine Simulation

2.1 Introduction

The model used for this study is based on a zero-dimensional, thermodynamic simulation of a turbocharged diesel engine (Assanis and Heywood 1986). The parent code, which has been validated against test results from several turbocharged diesel engines, was previously modified to allow for various levels of oxygen enrichment in the intake air and for operation with water-emulsified fuels (Assanis et al. 1990). This section briefly summarizes the main assumptions of the simulation and system submodels. Additional details on the parent code can be found in Assanis and Heywood (1986).

2.2 Basic Assumptions about System Models

2.2.1 Reciprocator Engine Model

The reciprocator simulation is a mathematical model of the processes occurring in the direct-injection four-stroke diesel engine. Figure 2.1 illustrates the overall system. The diesel four-stroke cycle is treated as a sequence of continuous processes: intake, compression, combustion (including expansion), and exhaust. In the reciprocator simulation, the system of interest is the instantaneous contents of a cylinder (i.e., air, fuel, and combustion products). In general, this system is open to the transfer of mass, enthalpy, and energy in the form of work and heat. Throughout the cycle, the cylinder is treated as a variable volume plenum, spatially uniform in pressure. Furthermore, the cylinder contents are represented as one continuous medium by defining an average equivalence ratio and temperature in the cylinder at all times.

Gas properties are calculated with the assumption of ideal gas behavior. At low temperatures (below 1000 K), the cylinder contents are treated as a homogeneous mixture of nonreacting ideal gases. At high temperatures (above 1000 K), the properties of the cylinder contents are calculated by assuming the burned gases are in equilibrium, with allowance for chemical dissociation (Martin and Heywood 1977). Provisions are incorporated in the thermodynamic property routines in order to model intake air with various levels of oxygen enrichment (i.e., with a desired N:O ratio). Equations for the conservation of mass and energy are developed for the contents of an open thermodynamic system. The conservation equation for the fuel mass is used to develop a differential equation for the change in fuel-air equivalence ratio of the system. The energy conservation equation is developed to obtain a differential equation for the change in temperature of the thermodynamic system. The details of the conservation of mass and energy equations can be found in Assanis (1991).

Quasi-steady, adiabatic, one-dimensional flow equations are used to predict mass flows past the intake and exhaust valves. The compression process is defined to include the ignition delay period (i.e., the time interval between the start of the injection process and the ignition point). The total length of the ignition delay can be either specified or predicted by using an

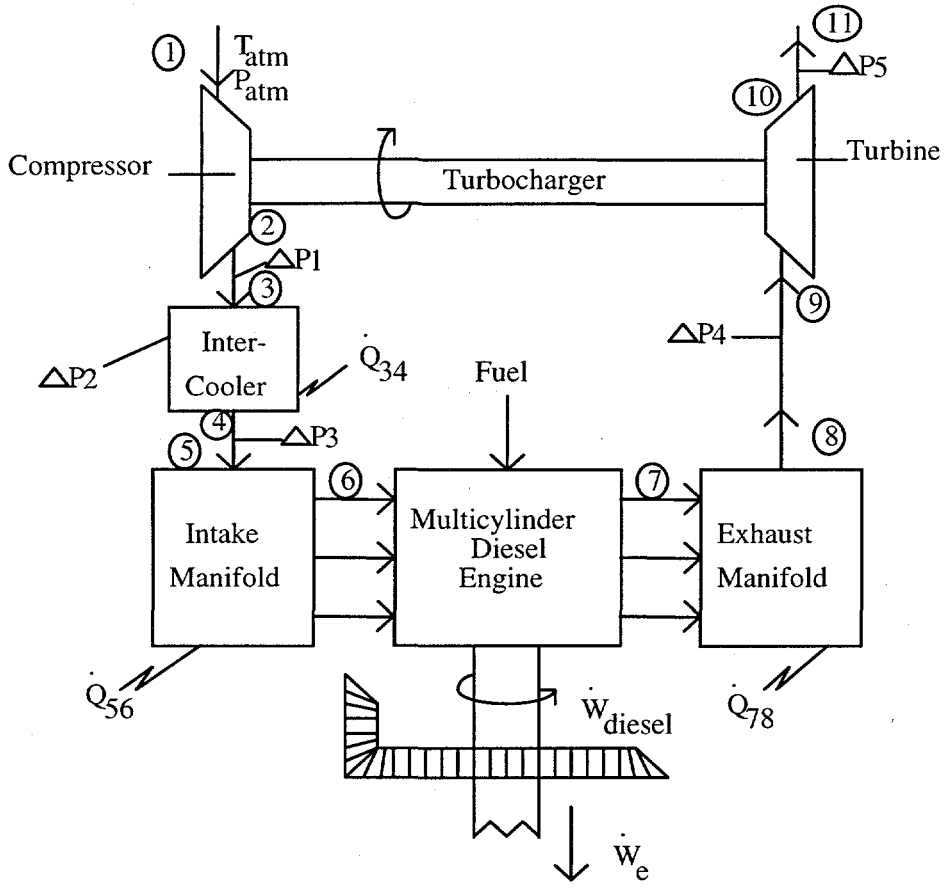

FIGURE 2.1 Turbocharged Diesel System Configuration

Arrhenius expression that is based on the mean cylinder gas temperature and pressure during the delay period. Combustion is modeled as a uniformly distributed heat-release process. The rate of heat release is specified by using an algebraic burning rate correlation. Heat transfer is included in all the engine processes. Convective heat transfer is modeled by using available engine correlations that are based on turbulent flow in pipes. The characteristic velocity and length scales required to evaluate these correlations are obtained from a model for mean and turbulent kinetic energy. Radiative heat transfer, based on the predicted flame temperature, is added during combustion.

2.2.2 Other Component Models

Engine friction submodels are included to obtain brake quantities from the computed reciprocator-indicated performance quantities. The reciprocator engine model calculates the state variables in one master cylinder of a multicylinder engine, while the manifolds and the other component models have inherent multicylinder capability. The coupling between the various cylinders and the turbocharger takes place in the manifolds; the latter are treated as plenums, which are filled and emptied as a function of time by the flows in and out. To simulate the effect of additional cylinders on the manifold conditions, and hence on the entire system behavior, the

conditions in the other cylinder are assumed to vary as echoes of the master cylinder, shifted by the appropriate phase angles. Manifolds are treated as constant-pressure and -temperature plenums; in addition, the option exists of determining these conditions from the solution of the manifold state equations. Intake and exhaust gas can be modeled as ideal gases. There is perfect and instantaneous mixing of all mass flows that enter each manifold with the gases in the manifold. This implies that there is no spatial variation in properties within a manifold at any instant of time, and all flows leaving a manifold have the properties of the manifold contents. The connecting pipes to and from the manifold are included as parts of the manifold. Empirical correlations are used to calculate instantaneous heat-transfer rates from the gas to the walls, as well as pressure losses. Conduction through the walls is modeled as axially symmetric. The boundary conditions on the outside wall surface of each component are specified.

2.3 Modeling of Reciprocator Engine Processes

2.3.1 Gas Exchange

A one-dimensional, quasi-steady, compressible-flow model is used to calculate the mass flow rates through the intake and exhaust valves during the gas exchange process. The intake manifold and the exhaust port are treated as plenums with known pressures. Furthermore, the temperature and average equivalence ratio of the intake charge (fresh air at intake manifold conditions) and the exhaust charge (mixture of air and combustion products at cylinder conditions) are known. When reverse flow into the intake manifold occurs, a rapid-mixing model is used (i.e., instantaneous mixing between the back-flowing charge and the intake charge is assumed).

At each step of the gas exchange process, values for the valve open areas and discharge coefficients are obtained from tabulated data. Given the open area, the discharge coefficient, and the pressure ratio across a particular valve, the mass flow rate across that valve is calculated from

$$\dot{m} = c_d A \frac{p_o}{RT_o}\left(\gamma R T_o\right)^{1/2}\left\{\left(\frac{2}{\gamma-1}\right)\left[\left(\frac{P_s}{P_o}\right)^{2/\gamma}-\left(\frac{p_s}{p_o}\right)^{(\gamma+1)/\gamma}\right]\right\}^{1/2} \qquad (2\text{-}1)$$

where c_d is discharge coefficient; A is valve open area; p_o is stagnation pressure upstream of restriction; p_s is static pressure at restriction; T_o is stagnation temperature upstream of restriction; γ is ratio of specific heats; and R is gas constant.

When the kinetic energy in the cylinder is negligible, the stagnation pressure and temperature reduce to the static pressure and temperature, respectively. For the case of choked flow, Equation 2-1 reduces to

$$\dot{m} = c_d A \frac{p_o}{RT_o}\left(\gamma R T_o\right)^{1/2}\left(\frac{2}{\gamma+1}\right)^{(\gamma+1)/2(\gamma-1)} \tag{2-2}$$

The mass, m(t), in the cylinder at any time t can be found from integration of the mass conservation equation, i.e.,

$$m(t) = m_o + \int_{t_o}^{t} \dot{m}_{in}\,dt - \int_{t_o}^{t} \dot{m}_{ex}\,dt \tag{2-3}$$

where m_o is mass in the cylinder at cycle start (IVO).

2.3.2 Ignition Delay Model

The ignition delay period in a diesel engine is defined as the time (or crank angle) interval between the start of fuel injection and the start of combustion. Both physical and chemical processes must take place before the injected fuel can burn. The physical processes are the atomization of the liquid fuel jet, the vaporization of the fuel droplets, and the mixing of the fuel vapor with air. The chemical processes are the precombustion reactions of the fuel, air, residual-gas mixture that lead to autoignition. These processes are affected by engine design and operating variables and by the fuel characteristics.

Ignition delay data from fundamental experiments in uniform-air environments are usually correlated by equations of the form

$$ID = A\, p^{-n} \exp(E/RT) \tag{2-4}$$

where ID is ignition delay, ms; E is apparent activation energy for the fuel autoignition process; R is universal gas constant; p is gas pressure, atm; T is gas temperature, K; and A and n are constants dependent on the fuel and the injection and airflow characteristics. Representative values for A, n, and E are given by Igura et al. (1975), Stringer et al. (1970), and Spadaccini and TeVelde (1980). In diesel engines, however, pressure and temperature change considerably during the delay period due to the compression resulting from piston motion. To account for these changing conditions, our ignition delay model predicts the start of combustion by integrating the reciprocals of instantaneous estimates of the ignition delay, based on Equation 2-4, until the following relationship is satisfied:

$$\int_{t_{inj}}^{t_{ign}} \frac{dt}{ID(t)} = 1 \tag{2-5}$$

2.3.3 Combustion Model

The diesel combustion process is a complex, unsteady, heterogeneous, three-dimensional process. Although an adequate conceptual understanding of diesel combustion has been developed, a comprehensive quantitative model that includes all the critical individual processes has yet to be proposed. An additional source of complication arises because the effects of oxygen content on combustion kinetics have not been adequately modeled. A useful approach to the problem of combustion simulation has been to model combustion as a heat-release process, as originally proposed by Lyn (1962).

An alternative approach to combustion modeling is to describe the apparent fuel burning rate by algebraic expressions. The parameters appearing in these expressions can then be chosen suitably to reproduce the dependence of the actual fuel burning rate on engine type and particular operating conditions. Watson et al. (1980) developed such a model, where a nondimensional apparent fuel burning rate, $M(\tau)$, is expressed as the sum of two components, one related to premixed and the other to mixing or diffusion-controlled burning, i.e.,

$$M(\tau) = \beta M_p(\tau) + (1-\beta)\, M_d(\tau) \tag{2-6}$$

where the premixed burning distribution is

$$M_p(\tau) = C_{p1}\, C_{p2}\, \tau^{(Cp1-1)}\, (1 - \tau^{Cp1})^{(Cp2-1)} \tag{2-7}$$

and the diffusion-controlled burning distribution is

$$M_d(\tau) = C_{d1}\, C_{d2}\, \tau^{(Cd2-1)}\, \exp(-C_{d1}\, \tau^{Cd2}) \tag{2-8}$$

where β is a phase proportionality factor expressing the cumulative fuel burned by premixed burning as a fraction of the total fuel injected; C_{p1}, C_{p2}, C_{d1}, and C_{d2} are shape factors that can be determined as a function of the engine operating conditions. Using data from three typical turbocharged truck engines, Watson (1980) established the following correlations:

$$\begin{aligned} \beta &= 1 - a\, \phi_{ove}^{\,b} / ID^c \\ C_{p1} &= 2.0 + 1.25 \times 10^{-8} (ID \times N)^{2.4} \\ C_{d1} &= k_1\, \phi_{ove}^{\,-k2} \\ C_{d2} &= k_2\, C_{d1}^{\,k4} \end{aligned} \tag{2-9}$$

where ID is ignition delay, ms; N is engine speed, r/min; ϕ_{ove} is the overall cylinder equivalence ratio; and a, b, c, k_1, k_2, k_3, and k_4 are constants that must be adjusted for each combustion chamber design. Appropriate constants for the GE locomotive diesel engine of our study were established during the model calibration phase and are given below:

$$a = 1.362;\ b = 0.65;\ c = 0.08;\ k_1 = 30.0;\ k_2 = 0.6;\ k_3 = 0.962;\ k_4 = 0.262;\ C_{p2} = 110{,}000 \tag{2-10}$$

Based on our earlier work (Assanis et al. 1993), Watson's combustion model failed to reproduce the diffusion burning phase when the engine was supplied with oxygen-rich combustion air. In particular, the correlation could not fit the gradual drop of the heat-release rate observed in the combustion tail. This can result in significant errors, if this heat-release model is to be implemented in an engine simulator.

For this work, a heat-release correlation that was developed earlier (Assanis et al. 1993) on the basis of experimental data for oxygen-enriched diesel combustion was used, i.e.,

$$\frac{\dot{m}_{f,b}(\theta)}{m_{f,0}} = \theta^{Bp} \cdot \exp\left(A_p - C_p \cdot \sqrt{\theta}\right) + \theta^{Bd} \cdot \exp\left(A_d - C_d \cdot \sqrt{\theta}\right) \qquad (2\text{-}11)$$

where $\dot{m}_{f,b}$ is the instantaneous rate of fuel burning; $m_{f,o}$ is the total mass of fuel injected; θ is the crank angle after ignition; A, B, C, and D are adjustable parameters; and subscripts p and d correspond to the premixed and diffusion combustion phases, respectively. The adjustable parameters are determined by matching the experimental heat-release rates against curve-fitted profiles generated by using the above heat-release correlation (Equation 2-11). On the basis of measured heat-release data for a Caterpillar, single-cylinder diesel engine (Assanis et al. 1993) operating with an oxygen content in the range of 21% to 35% by volume and an overall equivalence ratio of about 0.5, the following values are recommended for the constants:

$$\begin{aligned} A_p &= 16.81 - 0.61539\ \%\ O_2 \\ B_p &= 26.625 - 0.70921\ \%\ O_2 \\ C_p &= 28.152 - 0.76602\ \%\ O_2 \\ A_d &= -6.0295 - 0.1692\ \%\ O_2 \\ B_d &= 3.4698 + 0.10564\ \%\ O_2 \\ C_d &= 1.8202 + 0.03195\ \%\ O_2 \end{aligned} \qquad (2\text{-}12)$$

2.3.4 Turbulent Flow Model

The heat-transfer model of the cycle simulation requires estimates of the characteristic velocity and length scales. To estimate these scales in a way that incorporates the key physical mechanisms affecting charge motion in the cylinder, a turbulent flow model is used. This model is a variation of the models used by Mansouri et al. (1982) and Poulos and Heywood (1983) in previous engine simulation work.

The turbulence model consists of a zero-dimensional energy cascade. Mean flow kinetic energy, K, is supplied to the cylinder through the valves. Mean kinetic energy, K, is converted to turbulent kinetic energy, k, through a turbulent dissipation process. Turbulent kinetic energy is converted to heat through viscous dissipation. When mass flows out of the cylinder, it carries with it both mean and turbulent kinetic energy.

At any time during the cycle, the mean flow velocity, U, and the turbulent intensity, u′, are found from the knowledge of the mean and turbulent kinetic energies, K and k, respectively. Thus, the following equations apply:

$$K = \frac{1}{2} m U^2, \qquad k = \frac{3}{2} m u'^2 \tag{2-13a, b}$$

where the factor 3 in Equation 2-13b comes from assuming that the small-scale turbulence is isotropic (and accounting for all three orthogonal fluctuating velocity components).

The time rate of change of the mean kinetic energy, K, is given by

$$\frac{dK}{dt} = \frac{1}{2} \dot{m}_i V_i^2 - P - K \frac{\dot{m}_e}{m} \tag{2-14}$$

Similarly, the rate of change of the turbulent kinetic energy, k, is

$$\frac{dk}{dt} = P - m\varepsilon - k \frac{\dot{m}_e}{m} + A \tag{2-15}$$

with

$$\varepsilon = \frac{u'^3}{l} = \frac{(2k/3m)^{3/2}}{l} \tag{2-16}$$

where m is mass in the cylinder; m_i is mass flow rate into the cylinder; m_e is mass flow rate out of the cylinder; V_i is jet velocity into the cylinder; P is rate of turbulent kinetic energy production; ε is rate of turbulent kinetic energy dissipation per unit mass; A is rate of turbulent kinetic energy amplification due to rapid distortion; and l is characteristic size of large-scale eddies.

Assuming that turbulence production in the engine cylinder is similar to turbulence production in a boundary layer over a flat plate (Tennekes and Lumley 1972), we can express P as

$$P = \mu_t C_\beta (U/L)^2 \tag{2-17}$$

where $\mu_t = C_\mu k^2/(m\varepsilon)$ is turbulent viscosity; $C_\mu = 0.09$ is a universal constant; C_β is an adjustable constant; and L is a geometric length scale. Furthermore, the characteristic size of the large-scale eddies, l, and the representative geometric length scale, L will both be identified with the macro-scale of turbulence, assumed to be given by

$$l = L = V/(\pi B^2/4) \tag{2-18a}$$

where V is the instantaneous volume of the combustion chamber and B is the cylinder bore, subject to the restriction that

$$L \leq B/2 \tag{2-18b}$$

Hence, Equation 2-17 can be rewritten as

$$P = 0.3307\, C_\beta \left(\frac{K}{L}\right)\left(\frac{K}{M}\right)^{1/2} \tag{2-19}$$

During the compression and the combustion processes, the turbulent kinetic energy decays due to viscous dissipation. At the same time the turbulent kinetic energy is amplified due to the rapid distortion that the cylinder charge undergoes with rising cylinder pressures. Consequently, an amplification term will be larger during combustion when the unburned gas is assumed to be compressed by the flame at a sufficiently high rate. However, in the diesel engine context of high compression ratios, the amplification term is included during compression, too.

Using Equation 2-13b, and after some manipulation, the rate of turbulence amplification due to rapid distortion can be expressed as

$$A = \frac{2}{3} k \frac{\dot{\rho}}{p} \tag{2-20}$$

2.3.5 Heat Transfer

The heat transfer mechanisms in a diesel engine include forced convection $(\dot{Q}_c)$ from the turbulent flow in the cylinder to the combustion chamber walls and radiation $(\dot{Q}_r)$ from the burning soot particles. The total heat transfer $(\dot{Q}_r)$ is therefore given by

$$\dot{Q}_w = \dot{Q}_c + \dot{Q}_r \tag{2-21}$$

The convective heat transfer at the gas-to-cylinder wall interface depends on the temperature gradient in the boundary layer at the surface. However, due to inherent difficulties in calculating the details of turbulent fluid motion in the combustion chamber during the operating cycle of the engine, the convective heat-transfer rate is usually expressed as

$$(\dot{Q}_c) = h\, A\, (T_g - T_w) \tag{2-22}$$

where h is convective heat-transfer coefficient, and A is surface area of cylinder head, piston, liner, as appropriate. Usually the convective heat-transfer coefficient is calculated from a Nusselt-Reynolds number correlation analogous to that used for steady turbulent flow in a pipe (Woschni 1967; Annand and Ma 1971; Sitkei 1974; Kamel and Watson 1979), i.e.,

$$N_u = a\, Re^d \tag{2-23}$$

where $N_u = hL/\lambda$ is the Nusselt number; $Re = VL/\nu$ is the Reynolds number; L is a characteristic length; V is a characteristic velocity; λ is thermal conductivity; ν is kinematic viscosity; and a, d are constants adjusted to fit experimental data.

To calculate the convective heat-transfer coefficient from Equation 2-23, instantaneous values for the characteristic length and velocity scales, and the gas transport properties, are needed. Representative values of the characteristic length and velocity scales, and the gas temperature, pressure, and equivalence ratio at which the gas properties are to be evaluated, are used. For our heat-transfer model, the characteristic length scale is take to be the macro-scale turbulence, as defined by Equations 2-18a,b. The characteristic velocity V is postulated to be an effective velocity due to contributions from the mean kinetic energy, the turbulent kinetic energy, and piston motion, i.e.,

$$V = [\, U^2 + u'^2 + (V_p/2)^2 \,]^{1/2} \tag{2-24}$$

where U is mean flow velocity, u' is turbulent intensity, and Vp is instantaneous piston speed. While this expression for V is speculative, it is constructed in such a way that increases in any of the three component velocities lead to increases in the heat transfer rate, while at the same time errors due to overestimating the contribution from any one component are minimized.

Many attempts have been reported to determine the constants a and d, through curve-fitting experimental results (e.g., Annand 1963; Woschni 1967; Sitkei 1974; Kamel and Watson 1979). Suggested values are

$$\begin{aligned} a &= 0.035 \text{ to } 0.13 \\ d &= 0.7 \text{ to } 0.8 \end{aligned} \tag{2-25}$$

depending on intensity of charge motion. The gas density and transport properties are evaluated at the mean gas temperature, pressure, and equivalence ratio of the cylinder contents.

Radiative heat flux is significant in diesel engines. However, due to the difficulty of measuring instantaneous flame temperature and heat flux, it is not easy to quantify the contribution of radiation to the overall heat transferred. Estimates of the relative importance of radiation have varied between a few and 30 percent of total heat transfer, and vary according to engine type (Annand 1963; Ebersole et al. 1963; Annand and Ma 1971; Oguri and Shigewo 1972; Flynn et al. 1972; Kunitomo et al. 1974; Dent and Suliaman 1977).

Assanis and Heywood (1986) proposed that the instantaneous radiant flux be expressed as

$$Q_r = \varepsilon_a\, \sigma\, A\, (T_r^4 - T_w^4) \tag{2-26}$$

where ε_a is apparent gray-body emissivity, σ is Stephan-Boltzman constant, A is surface area, and T_r is apparent radiant temperature. Flynn's (1972) data suggest that the apparent radiant temperature is close to the adiabatic flame temperate during the period of peak heat release. However, as combustion progresses and relatively fewer close-to-stoichiometric fuel-air zones are found in the cylinder, this adiabatic flame temperature becomes considerably higher than Flynn's apparent radiant temperature. A better estimate of the apparent radiant temperature was found to be the mean of the adiabatic flame temperature and the average bulk gas temperature, i.e.,

$$T_r = \frac{T_g + T(\phi = 1.1)}{2} \tag{2-27}$$

The adiabatic flame temperature is modeled as the temperature of slightly greater than stoichiometric zones of hydrocarbon-air combustion products, i.e., T (ϕ = 1.1). The latter temperature is computed as a function of the instantaneous air temperature and pressure from a correlation obtained by applying a least-square curve-fitting technique to the results of the NASA equilibrium program for constant-pressure hydrocarbon-air combustion (Svehla and McBride 1973). The apparent emissivity is assumed to vary linearly between its maximum value (taken as 0.9) and zero over the duration of the expansion process.

2.3.6 Wall Conduction Model

The rates of heat transfer from the combustion gas to the walls of the various system components depend on the instantaneous difference between the gas and wall temperatures. Estimates of these wall temperatures have been calculated (e.g., Streit and Borman 1971) on the basis of the following assumptions: (1) each heat-transfer surface of interest is at a uniform surface temperature, (2) the heat-transfer surface temperatures are constant throughout the engine cycle, and (3) heat transfer by conduction through the walls is treated on a one-dimensional basis.

The assumption of constant wall temperatures over the engine operating cycle is reasonable for engines with high-conductivity metal walls and forced-convection jacket cooling. Measurements by LeFeuvre (1969) and Whitehouse (1971) on conventional engines have suggested that cyclic surface temperature variations are fairly small, ranging from 5 to 15 K. However, for engine surfaces insulated with low-conductivity materials, such as ceramics, surface temperature variations are more critical (Morel et al. 1985; Assanis 1985).

2.3.7 Friction Model

To convert indicated reciprocator performance quantities to brake performance quantities, engine friction calculations are required. Direct motoring of an engine is the common method of measuring friction, but the motoring losses are not the same as the losses under firing conditions. Reasons for this disparity include the lower pressure acting on piston rings and bearings; the lower temperatures of the piston and cylinder bore surfaces, and thus, the greater oil viscosity; the greater running clearance of the piston; and the missing exhaust blowdown period. Nevertheless, a breakdown analysis of motoring losses, supplemented by experiments on piston

and ring friction rigs, can be used to identify the relative importance of the many components of the total friction and their response to change in design variables. In general, the components of the losses, expressed in terms of mean effective pressure (mep), tend to fall into three groups:

1. Losses due to boundary lubrication, where the friction forces are approximately invariant with speed. These losses are undoubtedly influenced by the compression ratio.

2. Losses associated with hydrodynamically lubricated surfaces in relative motion, which vary directly with speed. All major rotating parts fall into this group.

3. Losses associated with fluid (air, water, and oil) pumping, which vary as the square of speed.

Therefore, the motoring losses can be expressed in the form

$$F = A + BN + CN^2 \tag{2-28}$$

where F signifies the losses in mep; N is engine speed; and A,B, and C are constants.

Millington and Hartles (1968) have measured motoring losses on a large variety of automotive diesel engines during the course of development of prototype engines. Their work suggests a readjustment of Equation 2-28, coupled with suitable selection of the constants, as follows:

$$F = A + 7.0\frac{N}{1000} + 1.5\left(\frac{V}{1000}\right)^2 \tag{2-29}$$

where F is motoring mep, psi; A is compression ratio minus 4 for DI diesel; N is engine speed, rpm; and V is mean piston speed, ft/min. Equation 2-29 represents a sound empirical correlation of the motoring loss data obtained from diesel engines. It is used to obtain brake quantities from the indicated quantities computed in the engine simulation.

2.3.8 NO Emission Model

The formation and destruction of thermal NO from atmospheric nitrogen has been studied widely on the basis of the extended Zel'dovich mechanism (Lavoie et al. 1970), i.e.,

$$\begin{aligned} O + N_2 &= NO + N \\ N + O_2 &= NO + O \\ N + OH &= NO + H \end{aligned} \tag{2-30}$$

For the purpose of implementing the NO kinetics model in the diesel simulation, the combustion chamber is divided into two zones: a burned zone (containing products of combustion) and an unburned zone (containing air and residual gas). At any instant throughout combustion, an incremental flux of fuel (given by Equation 2-11) that is accompanied by a stoichiometric flux of air is assumed to cross from the unburned zone to the burned zone. The products of combustion are assumed to be at the adiabatic flame temperature, resulting from combustion of a stoichiometric fuel-air mixture of specified oxygen content at the instantaneous unburned gas temperature and pressure (uniform within the combustion chamber). The kinetic rate of change of the concentration of NO in the postflame gases, along with appropriate expressions for its temperature-dependent rate constants, are obtained from Lavoie et al. (1970). The instantaneous concentrations of NO, O, O_2, OH, H, and N_2 are approximated by their equilibrium values at the specified burned zone temperature and pressure. On the basis of a knowledge of the instantaneous concentration of NO in the burned zone, its overall concentration in the cylinder can be computed by multiplying the ratio of moles in the stoichiometric burned core times the total number of moles in the cylinder.

2.4 Other System Component Models

A plenum model has been developed and incorporated into the code in order to model either a naturally aspirated engine or an engine with controllable intake/exhaust plenums. The plenum model can also be used to provide supercharging without requiring knowledge of turbomachinery maps. Ideal compressible-flow equations are used to model flow through each component, and isentropic efficiencies are defined to account for actual losses. The model is used to calculate the thermodynamic state within each plenum, which is needed to determine the mass flow rates past the valves of the master cylinder.

Both the intake and exhaust plenums are assumed to have large fluidic capacitance, so that variations in mass storage due to fluctuating flow rates into and out of the plenums can be neglected. Thus, a steady-state, steady flow is assumed to pass through the plenums and other turbomachinery components. The intake plenum temperature and pressure are specified at the start of the cycle and remain constant throughout the simulation. The intake plenum contains a single component gas (the fresh air charge from the compressor); thus, its thermodynamic state is completely defined.

The thermodynamic state of the exhaust plenum can be predicted by using either (1) a specified pressure model or (2) a specified turbomachinery efficiency model. For the first model, the exhaust plenum pressure, from which mass flow calculations across the exhaust valve are performed, needs to be specified. The specified efficiency model uses a first-law analysis to predict turbomachinery performance, given turbomachinery isentropic efficiencies. Application of the second model for a single-stage, turbocharged configuration is discussed below.

At the beginning of the calculations, initial estimates are made for the exhaust plenum pressure, exhaust turbine inlet pressure, and pressure losses across all turbomachinery connecting pipes. The plenum pressures are held constant throughout a cycle, and compressible-mass-flow equations are used to determine time-dependent flow rates across the valves of the master cylinder, based upon instantaneous cylinder pressure and effective valve throat areas. The time-dependent flow rates past the intake valve are averaged at the end of each engine cycle to obtain a cycle-averaged mass flow rate through the compressor, heat exchanger, and intake plenum. The specific heats and specific enthalpy of the compressor inlet flow are determined from the thermodynamic property routine during a preprocessing phase of the simulation (since compressor upstream pressure and temperature are user inputs and remain constant).

The downstream pressure of the compressor, P_2, is equal to the intake plenum pressure, P_5, plus the pressure drops across the intercooler and connecting pipes (refer to Figure 2.1). Thus, the power requirements of the compressor can be expressed as

$$\dot{W}_c = \frac{\dot{m}_i c_{pi} T_1 \left[P R_c^{(\gamma_1 - 1)/\gamma_1} - 1 \right]}{\eta_c} \tag{2-31}$$

where $PR_c = \frac{P_2}{P_1}$ is the compression ratio of the compressor, T is temperature of the flow, c_p is the constant-pressure specific heat, γ is the ratio of specific heats, η_c is the compressor isentropic efficiency, and $\dot{m}_j$ denotes cycle-averaged mass flow rate throughout the intake valve, intercooler, and compressor.

The enthalpy at the compressor outlet can readily be found if the compressor work and the inlet enthalpy are known. Next, an isentropic flow is assumed between the compressor outlet and intercooler inlet. The intercooler outlet enthalpy equals the intake plenum enthalpy. Any convective heat loss from the connecting pipe is modeled by using a Nusselt correlation for turbulent flow in pipes.

A similar analysis is performed on the exhaust side of the master cylinder. Instantaneous exhaust mass and enthalpy flow rates are calculated and used to determine cycle-averaged quantities that pass through the exhaust plenum, connecting pipes, and turbocharger turbine. The exhaust plenum exit enthalpy is found from the cycle-averaged enthalpy across the exhaust valve, corrected for the enthalpy drop across the exhaust plenum due to heat rejection. The turbine inlet enthalpy equals the plenum enthalpy minus the enthalpy drop due to heat rejection from the connecting pipe between the two components. The turbine inlet enthalpy is used to predict the new turbine inlet temperature, using an initial estimate of the constant-pressure specific heat.

The output power of the turbocharger turbine is used to drive the compressor after overcoming any mechanical losses between the two components. The mechanical losses are

accounted for by specifying a mechanical efficiency, η_m. Thus, the power required of the turbocharger turbine is

$$\dot{W}_t = \frac{\dot{W}_c}{\eta_m} \tag{2-32}$$

where $\dot{W}_c$ is determined from Equation 2-31. Alternatively, using compressible-flow relations, the turbocharger turbine power can be expressed as

$$\dot{W}_t = \dot{m}_e \eta_t c_{p9} T_9 \left[1 - PR_t^{(1-\gamma_9)/\gamma_9}\right] \tag{2-33}$$

where $PR_t = \frac{P_9}{P_{10}}$ is the turbine expansion ratio, $\dot{m}_e$ is the cycle-averaged exhaust mass flow, and η_t is the turbine efficiency. From the above two expressions for the turbine power, the turbine expansion ratio can be readily determined. Further, if the downstream pressure of the turbine is known, its upstream pressure can be determined and used to update the exhaust plenum pressure (by adding the pressure drop across the pipe connecting the turbine and exhaust plenum, ΔP_4). The downstream pressure of the turbine is simply the atmospheric pressure plus the pressure drop across the exhaust pipe, ΔP_5. The enthalpy exhausted to the atmosphere equals the turbine outlet enthalpy minus an enthalpy drop due to heat rejection from the exhaust pipe. This quantity is used to determine the overall energy balance of the system.

2.5 Method of Solution and Program Inputs and Outputs

2.5.1 Basic Method of Solution

The mass and energy conservation equations for the contents of an open thermodynamic system are applied in turn to the master reciprocator cylinder, the intake manifold, and the series of exhaust manifold sections. The individual submodels of the various system components and their thermodynamic and heat-transfer processes are brought together to form a complete system model. The result is a set of simultaneous, first-order ordinary differential equations. To perform predictive calculations with the cycle simulation, these equations must be integrated simultaneously over the full operating cycle. The integration is performed numerically, using a standardized predictor-corrector technique (Shampine and Gordon 1974). The code adjusts its order and step size internally to maximize efficiency and control the local error per unit step in a generalized scene.

2.5.2 Program Inputs and Outputs

The computer code is written in standard FORTRAN-77 and has been successfully executed on Hewlett-Packard 9000, Cray 2 mainframe, VAX and Micro-VAX systems (running VMS), and both Macintosh and IBM personal computers.

The input parameters that must be specified for each cycle simulation include system configuration, system dimensions and design parameters, wall structure specifications, systems operating conditions, initial conditions of the system, and certain computational parameters. From this information, the simulation program can predict the performance of the total engine system under a wide range of operating conditions.

The output includes detailed information about the state of the total system as a function of crank-angle throughout each engine cycle, as well as integrated performance results. Predicted performance results include power, specific fuel consumption, volumetric and thermal efficiencies, gross indicated and pumping mean effective pressure, total heat loss through each component, and results of an overall energy balance.

3 Air Separation Membrane

3.1 Operating Principle

Air delivered to engines can be enriched in oxygen by selective permeation through nonporous, polymeric membranes via a well-known "solution-diffusion" mechanism. In this mechanism, air molecules dissolve into the membrane and then diffuse across it. A typical membrane process for air separation is shown in Figure 3.1. The air, fed to the membrane device at elevated pressure, passes across one side of the membrane. The opposite side of the membrane is held at a lower pressure. The pressure differential across the membrane provides the driving force for the diffusion of oxygen and nitrogen across the membrane. Oxygen can diffuse more rapidly and become enriched in the low-pressure permeate stream, while nitrogen is concentrated in the retentate stream. With the membrane module constructed similar to a shell-and-tube-type heat exchanger, thousands of square feet of membrane area can be packed into one cubic foot (0.03 m^3) of pressure vessel volume.

3.2 Membrane Operating Modes

Air separation membrane units can be operated in one of three modes (as illustrated in Figure 3.2): vacuum, pressure, or mixed mode. In the vacuum mode, the feed air is pressurized to only slightly above atmospheric pressure (about 1 to 3 psig), and a vacuum is maintained on the permeate side of the membrane. The retentate is vented at atmospheric pressure. The vacuum mode is typically more energy-efficient than the pressure mode, primarily because a vacuum is applied only on the permeate (product stream). However, because of the limited differential

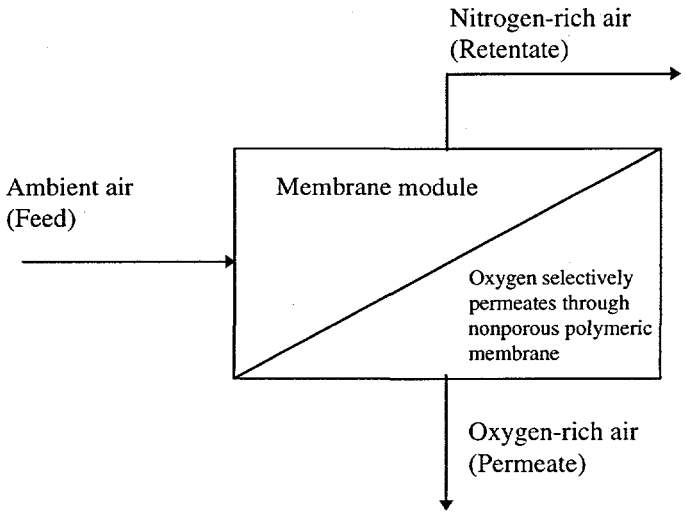

FIGURE 3.1 Basic Membrane Process for Air Separation

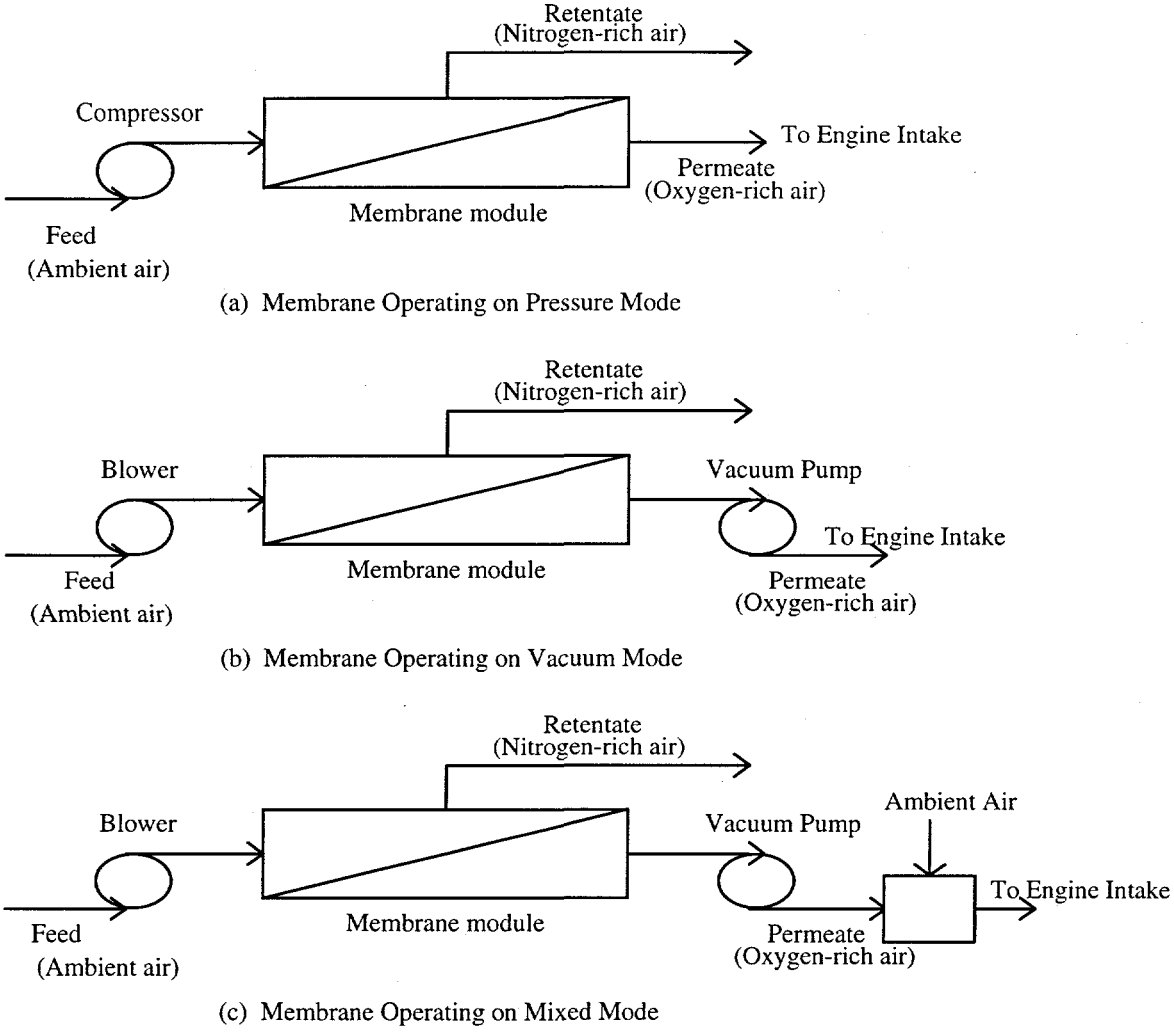

FIGURE 3.2 Air Separation Membrane Modes of Operation

pressure, the vacuum mode requires a larger membrane area for a given flow rate than does the pressure mode. In the pressure mode, the feed air is typically pressurized (by an air compressor) to several atmospheres, while the permeate is maintained at about atmospheric pressure. Higher driving forces are obtained in this mode because the differential pressures are higher than those of the vacuum mode, resulting in reduced membrane area requirements. However, the pressure mode is more energy-intensive, because both permeate and retentate have to be compressed to higher pressures. Finally, in the mixed mode, the feed air is pressurized, and a partial vacuum is maintained on the permeate side to increase both the compression ratio and differential pressure, and thus, the oxygen concentration. The oxygen-enriched air stream from the permeate is then mixed with an ambient air stream to obtain the desired air flow and oxygen concentration. Figure 3.3 illustrates how a separation membrane operating in the mixed mode would be retrofitted on a turbocharged, multicylinder diesel engine to enrich the oxygen content of the air delivered to its turbocharger compressor.

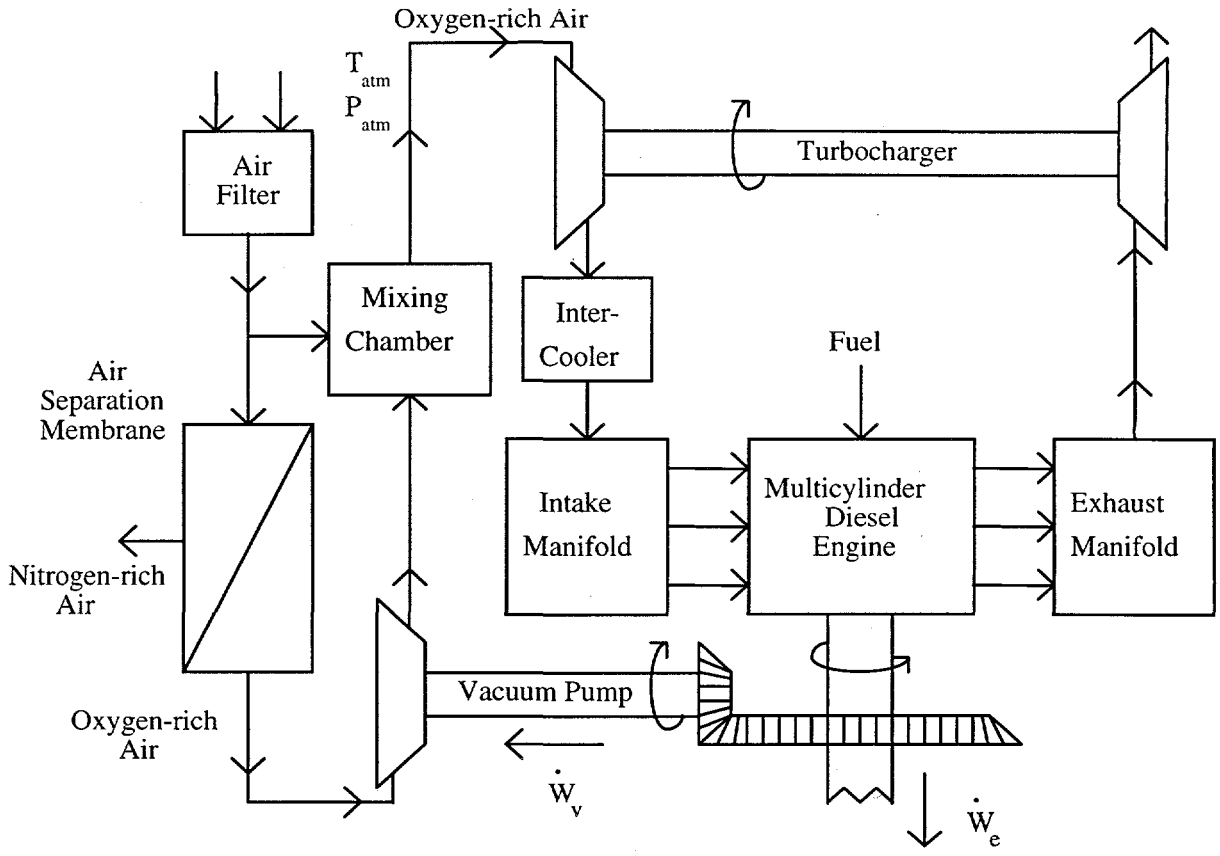

FIGURE 3.3 Turbocharged Diesel System Configuration Using Oxygen-Rich Air Supplied by Air Separation Membrane

3.3 Performance Characteristics

The performance of an air separator depends on the membrane's intrinsic properties and on several other parameters, such as membrane polymer structure, skin thickness, geometry of the fibers, fiber dimensions, flow pattern, feed direction, feed conditions, cartridge type, packaging density, and arrangement of separators. (Details are provided in Winston Ho and Sirkar 1992; Baker et al. 1990; and Koros and Chern 1987.) The selection of a membrane to achieve the desired oxygen-enriched air flow is evaluated in terms of the power required to maintain the differential pressure across the membrane and the amount of space it occupies. The following sections briefly summarize the influence of certain key parameters on the performance of air separation membranes.

3.3.1 Intrinsic Properties

The performance of a membrane is characterized by its permeability and selectivity (intrinsic properties) and stage cut (or recovery). The permeability, P_r, of a given gas is an intrinsic property of the membrane. It is closely associated with Henry's law for simple,

noninteracting gases, and for low concentration levels, and is given by (Gollan et al. 1985; Ragland et al. 1989)

$$P_{ri} = S_i \times D_i \tag{3-1}$$

where P_r is intrinsic permeability of gas 'i' in the membrane, cm^3 (STP) cm/cm^2-s-cm-Hg; S_i is the solubility of gas 'i' in the membrane, cm^3 (STP)/ cm^3 cm-Hg; and D_i is the diffusivity of gas 'i' in the membrane, cm^2/s. The overall permeability, a function of flow as well as of membrane composition, can be described by Fick's law as follows:

$$N_i = \frac{P_{ri} A \Delta P}{\delta} \tag{3-2}$$

where N_i is the flow rate of gas i (cm^3 of STP/s); P_{ri} is the intrinsic permeability of gas i in the membrane (cm^3 of STP-cm/cm^2-s-cm of Hg); A is membrane area (cm^2); δ is the membrane separating barrier thickness (cm); and ΔP is the trans-membrane partial pressure difference of gas i (cm of Hg).

Equation 3-2 clearly indicates that the degree of separation between the gases depends on the relative permeabilities of the gases to be separated. This ratio of gas permeabilities is known as selectivity or separation factor. The separation factor (α) between oxygen and nitrogen can be calculated as follows:

$$\alpha = \frac{P_{rO}}{P_{rN}} \tag{3-3}$$

The larger the value of the separation factor is, the better is the separation. The stage cut (φ or recovery) of an air separator is another important measure of performance; it is simply the permeate flow divided by the feed flow rate.

3.3.2 Polymer Structure

Polymeric solution-diffusion membranes for gas separation depend on the chemistry of the polymers and its influence on the rate at which gas molecules diffuse through the membrane. Rubbery and glassy polymers are the two classes of conventional materials used for gas separation. A rubbery polymer is an amorphous polymeric material that is above its softening or glass transition temperature under the conditions of use. These materials generally possess high permeability and low selectivity. A glassy polymer is an amorphous polymeric material that is below its softening or glass transition temperature under the conditions of use. Due to the more restricted segmental motions in glassy polymers, these materials offer enhanced selectivity with respect to rubbery polymers. As a result of growing interest in gas separation membranes, a host of new materials (grouped as polycarbonates and polymides) has been developed that are specifically designed to enhance gas permeability and selectivity. Gas membrane manufacturers are also vigorously pursuing development of new materials having superior properties. For

example, Perfluoro-2-2-dimethyl-1-3 dioxole copolymerized with tetrafluoroethylene, being developed at Compact Membrane Systems, Inc. (CMS), represents a new family of glassy membrane materials with high oxygen permeability and good selectivity for oxygen/nitrogen (Nemser et al. 1991). Dow has recently patented a series of halogenated polycarbonates and polyestercarbonates that have high O_2/N_2 selectivities (e.g., Anand et al. 1989).

3.3.3 Skin Thickness of Membrane Coating

For compact modules, the skin thickness of a membrane coating on a porous support (hollow fibers) is critical. The rate of gas transport across the membrane is inversely proportional to the skin thickness of the membrane (active) layer. When membrane material is coated over the porous support (hollow fibers), it is generally referred to as a composite membrane. The membrane must be mechanically strong to withstand pressure and temperature. For commercial membranes, skin thickness is typically on the order of 1000 to 2000 Å, with 400 to 1000 Å attainable in more finely tuned membranes. Apart from the skin thickness, the morphology of the membrane across the entire thickness also influences the ultimate performance of the membrane. Symmetric membranes (homogeneous) membranes have a uniform density across their thickness, while asymmetric membranes do not.

3.3.4 Fiber Dimensions

Flow loss in the fiber bore can be significant if the bore diameter is small and the permeate flow rate is high. In the case of hollow fiber geometry, the fiber size is an important factor with respect to packaging. Fiber sizes ranging from 50 to 1000 μ are currently available. Larger fiber sizes offer less tube flow restriction, but packaging density is low. There is a tradeoff between the packaging density and pressure drop across the fibers. The selection of fiber internal and outside diameters depends on the magnitude of the expected permeate flow rate per fiber, fabrication technology, and mechanical strength considerations.

3.3.5 Geometry and Membrane Cartridge Options

Two geometries are commonly used, flat films and hollow fibers. The membrane geometry influences the manner in which the membrane is packaged. Figure 3.4 shows a schematic of flat-film and hollow-fiber membranes. Hollow fibers offer excellent packaging compared to flat films. In contrast to flat membranes, hollow fibers are self-supporting. The inside and outside of the fibers are in the range of 100-500 μ and 500-1000 μ, respectively. The maximum external and internal pressures at which they can be operated are determined by the modules of the membrane material, the ratio of fiber OD and ID, and the detailed structure of the membrane.

Regardless whether the membrane is fabricated as a flat sheet or a hollow fiber, it must be incorporated into a useful "package" that is readily usable. A compact membrane cartridge design should have a high packaging density, because the permeate gas flow per unit membrane area is inherently low. Flat sheet, spiral-wound, and hollow-fiber geometries are the three

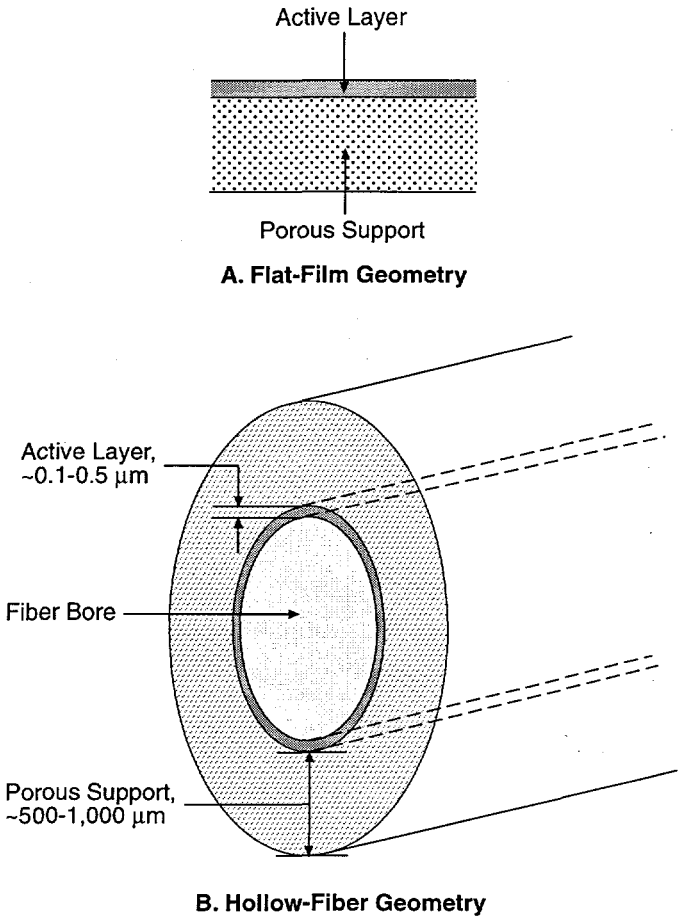

FIGURE 3.4 Geometries of the Gas Separation Membranes

membrane cartridge options available; each has its advantages and limitations. Flat sheet modules resemble plate-and-frame press filter. Figure 3.5 (Baker et al. 1990) shows the elements of plate-and-frame membrane module. The fabrication of such modules is relatively easy, but they give the lowest surface area per unit volume. Spiral-wound cartridges consist of a number of leaves, each containing two flat sheets of membrane separated by porous support material, as shown schematically in Figure 3.6 (Baker et al. 1990). Spiral-wound cartridges are reasonably compact, and system designs incorporating spirals require a simple pressure vessel. Such a cartridge provides area densities intermediate between the plate-and-frame and typical hollow-fiber modules. However, gas by-pass around the cartridges due to "brine seal" misalignment or failure within the pressure vessel is a potential concern that may reduce spiral-wound cartridge productivity. In the case of hollow fibers, small hollow-fiber bundles were sealed with an adhesive into header plates at opposite ends of the module in such a way that a large number of fibers could be included. The packing density of hollow-fiber cartridge is the highest by far, compared to the other two cartridges, and this cartridge is simple to operate and maintain on clean gas streams (Koros et al. 1987). Typically, a hollow-fiber membrane module resembles a shell-and-tube geometry. Figure 3.7 (Baker et al. 1990) illustrates the elements of a typical hollow-fiber membrane module.

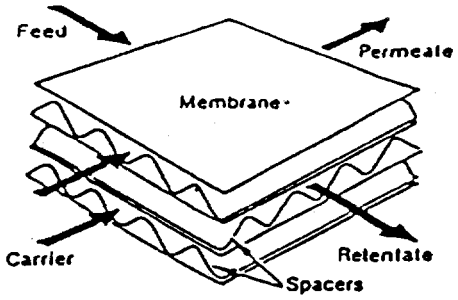

FIGURE 3.5 Elements of Plate-and-Frame Membrane Module

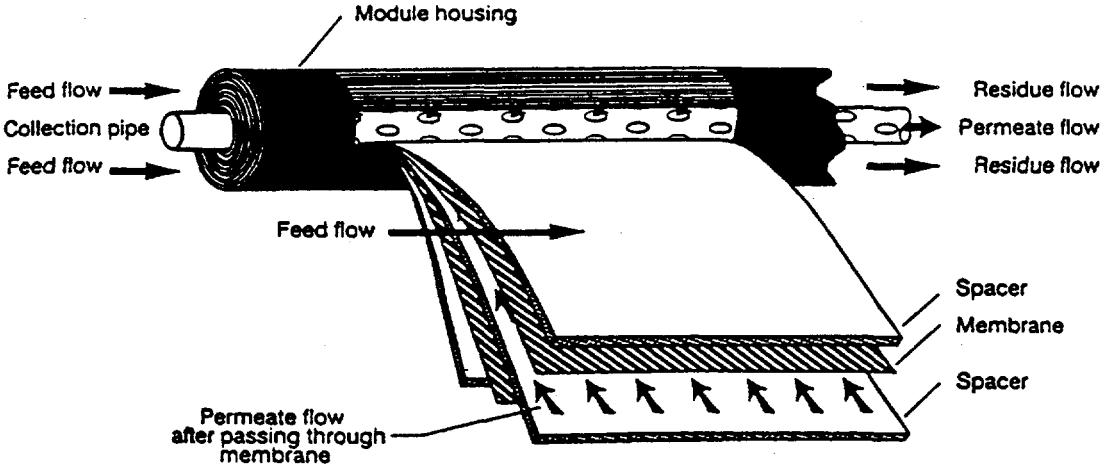

FIGURE 3.6 Elements of Spiral-Wound Membrane Module

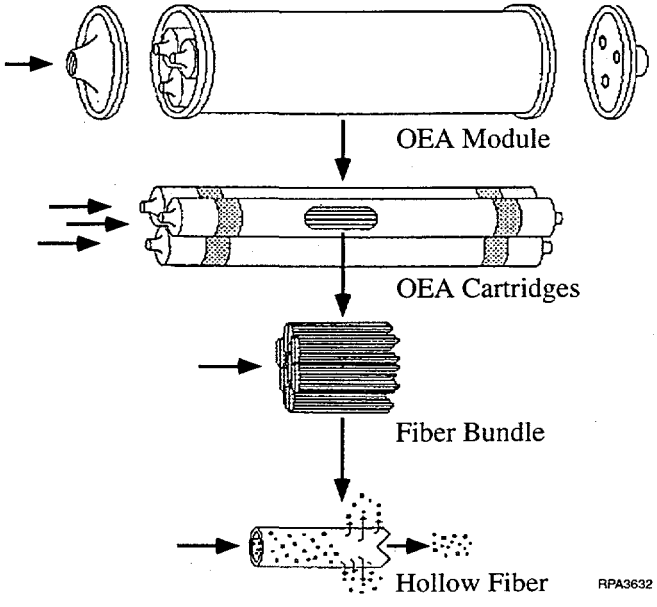

FIGURE 3.7 Typical Hollow-Fiber Membrane Module

3.3.6 Flow Patterns

The performance of the membrane separator is affected by the relative directions of feed and permeate flow in the vicinity of the active layer of the membrane and/or the relative flow directions of the bulk feed and permeate streams. The ideal flow patterns in a membrane are shown in Figure 3.8. The feed and permeate streams may be directed co-currently or counter-currently to one another. Crossflow permeation, with the permeate stream perpendicular to the membrane, may also be practiced. For co- and counter-current permeation, the gas in contact with the downstream side of the membrane consists of gas that has just permeated through the membrane, plus the bulk permeate that is flowing past it. For crossflow permeation, on the other hand, the permeate gas that is in contact with the active layer consists entirely of gas that has just passed through the membrane.

3.3.7 Feed Direction

In the shell-side feed permeators, the feed is brought in contact with the outer surface of the membrane fibers. Gas permeates into the fiber and then flows down the fiber bore, from which it passes through the tubesheet and out of the pressure vessel. In the tube-side feed permeators (for example, see Figure 3.9), the feed is delivered to the bore of the fibers. Two tubesheets are required, with feed gas being introduced through one tubesheet while nonpermeating gas exits from the other. The choice between shell-side and tube-side feed in hollow-fiber modules is generally made on the basis of the separation to be performed.

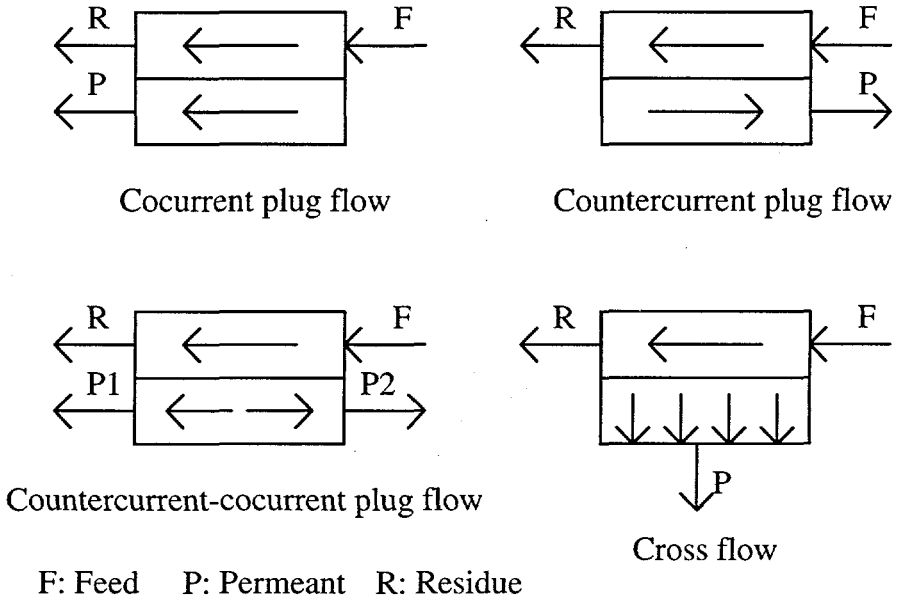

FIGURE 3.8 Ideal Flow Patterns in a Membrane Gas Separator

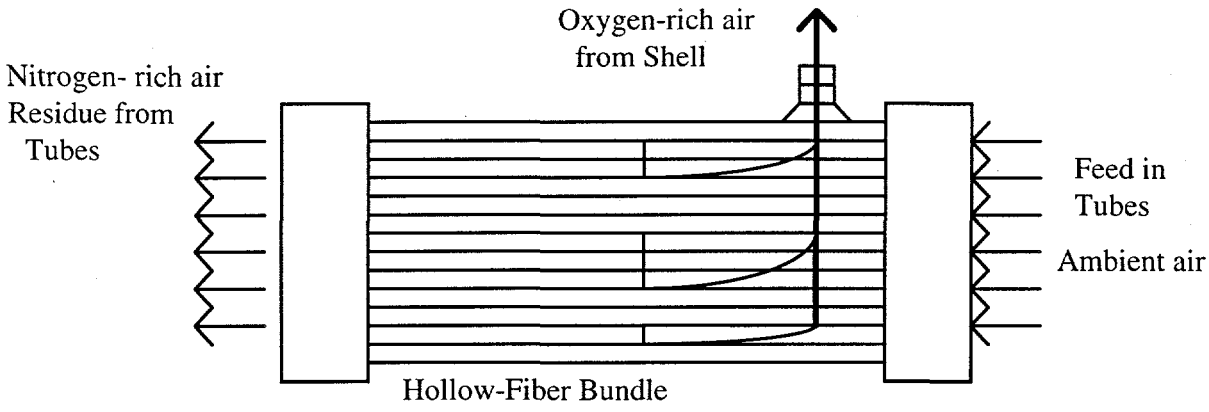

FIGURE 3.9 Schematic of a Counterflow Hollow-Fiber Membrane Module with Shell-and-Tube Geometry

3.3.8 Feed Conditions

Raising the feed pressure results in a higher-purity permeate product when the separator is operated at the same fractional stage cut (recovery), although the extent of the increase diminishes at higher feed pressures. Undoubtedly, an increase in the feed pressure will lower the membrane area needed for a given fast gas recovery. Temperature is also an important variable that directly affects physical properties of the membrane, and hence its permeation and selectivity. The temperature limits for membranes are related to the glass transition temperature of the polymer. The permeability (product of the solubility and mobility coefficients) tends to be dominated by the diffusivity and increases with increasing temperature. On the other hand, the separation factor is moderated in its temperature-dependence because the temperature dependencies of the permeabilities of the various gases are rather similar. The addition of humidity to the feed air does not appreciably affect the permeation because water vapor readily permeates the membrane. In comparing the permeability coefficients of H_2O, N_2, and O_2 for several polymers, the permeability of H_2O is at least two orders of magnitude greater than the permeability of either O_2 or N_2 (Brandup et al. 1975).

3.3.9 Arrangement of Separators

The manner in which gas permeators are arranged with respect to one another is determined by both the module design and the process application. To increase the product recovery beyond what can be provided by the once-through (single-stage) systems, the membranes must be operated with recycling (multistage). Recycling of the permeate causes the feed composition to the membrane to increase, which results in a higher product purity at any given recovery. Recompression of recycled permeate adds both investment and operating cost to the membrane system; however, membranes can still be competitive in these cases.

3.4 Model of an Air Separation Membrane

Various mathematical models and calculation methods for designing hollow-fiber membranes have been reported in the literature (Pan 1986, Chern et al. 1985). Typically, a permeator model includes (Winston Ho et al. 1992):

1. A relationship describing transport across the membrane.
2. Mass balance equations.
3. Relationships or assumptions for the pressure drops that occur on both sides of the membrane due to convective flow of gas.
4. Boundary conditions that reflect the configuration and operation of the permeator being modeled.

The above relationships lead to a set of differential equations that, when integrated numerically, yield the performance of the module. The development of a model to study all the performance variables and their tradeoffs would be quite exhaustive and beyond the scope of this effort. In the present work, a Du Pont proprietary code was made available to establish a relationship between the permeate oxygen concentration and stage cut under the specified input conditions listed in Table 3.1 and at several pressure ratios between the feed and permeate (ranging from 1.5 to 4), in the following form:

$$\%O_2 = A\varphi^3 + B\varphi^2 + C\varphi + D \qquad (3\text{-}4)$$

where % O_2 is the permeate oxygen concentration; A, B, C, and D are third-order polynomial coefficients as a function of the pressure ratio between the feed and permeate; and φ is the stage cut. Equation 3-4 was used to compute the stage cut at several desired permeate oxygen concentrations. Perfluoro-2-2-dimethyl-1-3 dioxole copolymerized with tetrafluoroethylene, being developed at CMS, is being considered as a membrane material (Nemser and Roman 1991) in the present model. From the stage cut, feed flow rates corresponding to the permeate flow rate and oxygen concentration can be computed. The pumping work can be computed from the pressure ratio between the feed and permeate and from the feed and permeate flow rates.

In the absence of certain key design data, including the mean partial pressure of oxygen in the module and the fiber geometry, it is difficult to estimate membrane size. However, an attempt was made to demonstrate the influence of membrane properties and other design variables on the membrane's size and power requirements. For purposes of comparison, a pressure ratio of 3.0 between the feed and permeate across the membrane was assumed, and the mixed mode was considered to be the mode of operation (the mixing stream's concentration was 28% by volume, and its flow was about 72% of the total engine air flow). The module size also varies with the active length of the fibers, which is, in turn, a function of pressure drop across the fiber tubes. For purposes of this study, the active length was arbitrarily selected to be 3 or 4 ft. Finally, to calculate the membrane surface area by using Equation 3-2, the end pressures of oxygen across the feed and permeate were employed instead of the mean partial pressure of oxygen. Membrane volume and module size were computed on the basis of fiber geometry and packing density.

TABLE 3.1 Membrane Properties and Input Parameters for Two CMS Materials

Property	CMS-3	CMS-7
Permeability (cm^3(STP)-cm/cm^2-s-cm Hg x 10^{10})		
Oxygen	340	990
Nitrogen	130	480
Water vapor	2000	4500
Selectivity (O_2/N_2)	2.71	2.05
Membrane skin thickness (μ)	0.1	0.1
Absolute pressure ratio between feed and permeate	1.5, 2.0, 3.0, 4.0	1.5, 2.0, 3.0, 4.0
Fiber geometry	Hollow	Hollow
Fiber dimensions (OD/ID) (μm)	660/500	660/500
Active fiber length (ft)	3,4	3,4
Packing density	0.5	0.5
Permeate pressure	ambient	ambient
Feed air pressure (in. Hg) for vacuum and mixed mode	2	2

4 Results and Discussion

4.1 Engine Configuration

To explore the effect of various oxygen-enrichment levels in the intake air on engine performance and emissions, a representative 12-cylinder, GE 12-7FDL locomotive diesel engine was selected, and the diesel engine simulation was applied to model its performance. The specifications of the engine geometry are given in Table 4.1. Locomotive diesel engines are operated at a series of fixed settings (throttle notches 1 through 8); each setting provides a constant amount of power at a governed engine speed. Turbomachinery maps were not available, so the intake and exhaust manifolds were treated as constant-pressure and -temperature plenums. The intake plenum conditions were specified; the exhaust plenum conditions were predicted by means of ideal thermodynamic models of the compressor and turbine with specified efficiencies. The actual intake and exhaust valve events and the manifold control volumes and surface areas were obtained from a previous study conducted at the Southwest Research Institute (Markworth et al. 1993).

4.2 Model Calibration and Validation

4.2.1 Model Matching with Watson's Heat-Release Correlation

Complete and reliable experimental engine data (specifically, pressure and heat release) were not available to utilize in matching the DES to the GE engine. However, another simulation code, TRANSENG, contained extensive information about the engine operating at full load (Notch 8). Hence, the matching was done by tuning the variables in the DES model at Notch 8. The first step in matching the DES code was to match the mass of air flowing through the engine during intake equivalent to that through actual engine. The next step was to tune the DES code

TABLE 4.1 Specifications for GE Locomotive Diesel Engine

Item	Value
Bore (mm)	228.6
Stroke (mm)	266.7
Connecting rod length (mm)	589.7
Compression ratio	12.7:1
Displacement volume (L)	10.9
Number of cylinders	12
Number of valves	48
Rated speed (rpm)	1050
Rated power (bhp)	2500
Standard injection timing (bTDC)	24

so that its heat-release rate predictions match the available rate prediction of the TRANSENG simulation. This was done to match the DES combustion process to that of the TRANSENG simulation, which had already been matched to the actual engine. The constants in Watson's phenomenological heat-release model were extensively investigated to adjust the shape of the heat-release rate profiles. A match was obtained between DES and TRANSENG when both had equivalent areas under the heat-release rate profiles (the same amount of energy had to come from equal amounts of fuel).

Figure 4.1 shows the heat-release rate profiles for both DES and TRANSENG, indicating the level of confidence obtained during the matching process. The friction constants were adjusted so that there was as little variation between DES predicted and actual experimental brake power when going from a full-load condition to a partial load while maintaining reasonable mechanical efficiency. At full load, the mechanical efficiency was tuned to 91%, and at part load, to 86%. Figure 4.2 illustrates the firing pressure trace of the DES prediction relative to the supplied Notch 8 experimental data. After the tuning was complete, it was desired to run the DES code and compare the results with both TRANSENG predictions and experimental results. The matching parameters at Notch 8 are shown in Table 4.2.

The TRANSENG code was able to predict the brake power to within 1.12%; however, the back pressure had to be lowered to 14.5% below the actual engine condition to obtain this value. In comparison, the brake power prediction by DES was higher by only 4.4% with all of the actual engine settings used as inputs, including the back pressure. On the basis of the results obtained in matching the DES predictions with experimental results at Notch 8, the tuning parameters and other input parameters are held constant through the study. Subsequently, the modified DES code has been extended to predict the performance at other notch positions (load and speed conditions), as well as the performance with oxygen-enriched intake air and fuel injection timing.

TABLE 4.2 Matching DES with TRANSENG and Experimental Data at Notch 8

				% Error	
Parameter	DES	TRANSENG	Engine	DES vs Engine	TRANSENG vs Engine
Input					
Engine speed (rpm)	1052	1052	1052	0	0
Fuel (g/cyl. per cycle)	1.0324	1.0324	1.0324	0	0
Intake manifold temp. (K)	360.1	360.1	360.1	0	0
Exhaust manifold temp. (K)	838.2	838.2	838.2	0	0
Intake manifold pressure (atm)	2.3958	2.3891	2.3958	0	-0.28
Exhaust manifold pressure (atm)	1.9189	1.6404	1.9189	0	-14.51
Volumetric efficiency (%)	136	-	136.2	0.15	-
Output					
brake power (bhp)	2603.7	2522	2494	4.4	1.12
bsfc (lb/bhp-hr)	0.331	0.3488	0.3454	-4.17	0.98
Air-to-fuel ratio	33.73	33.11	33.6	0.39	-1.46
Air flow (lb/s)	8.07	8.093	8.119	-0.60	-0.32

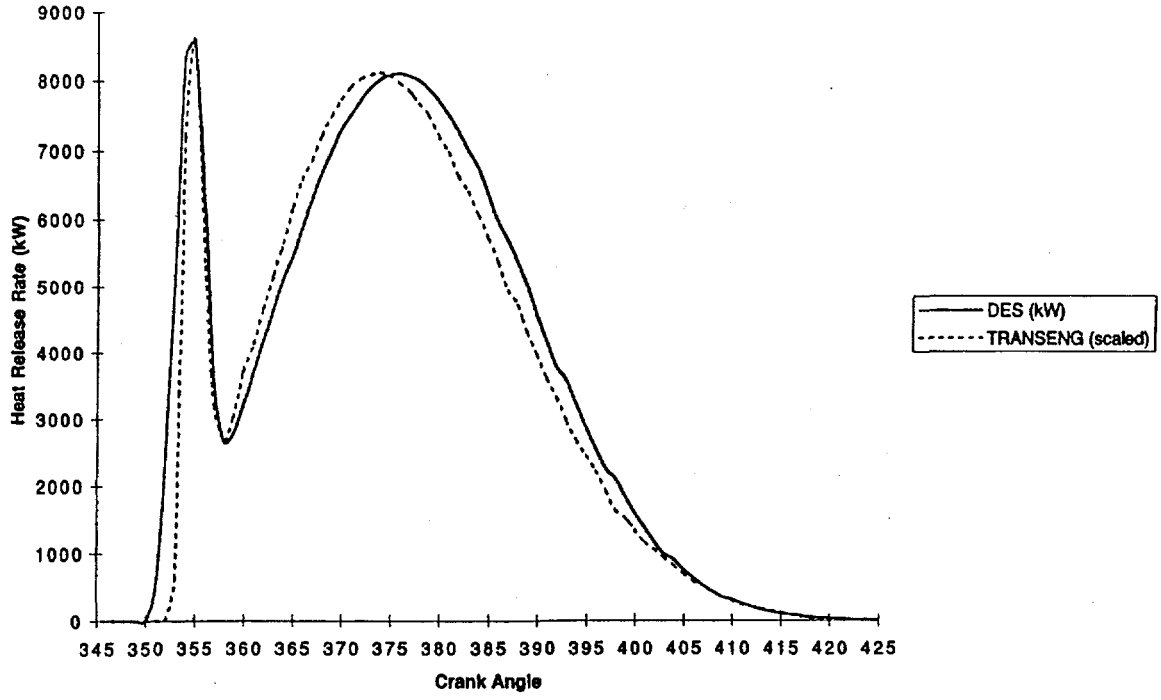

FIGURE 4.1 Diesel Engine Simulation (DES) and TRANSENG Heat-Release Profiles at Full Load

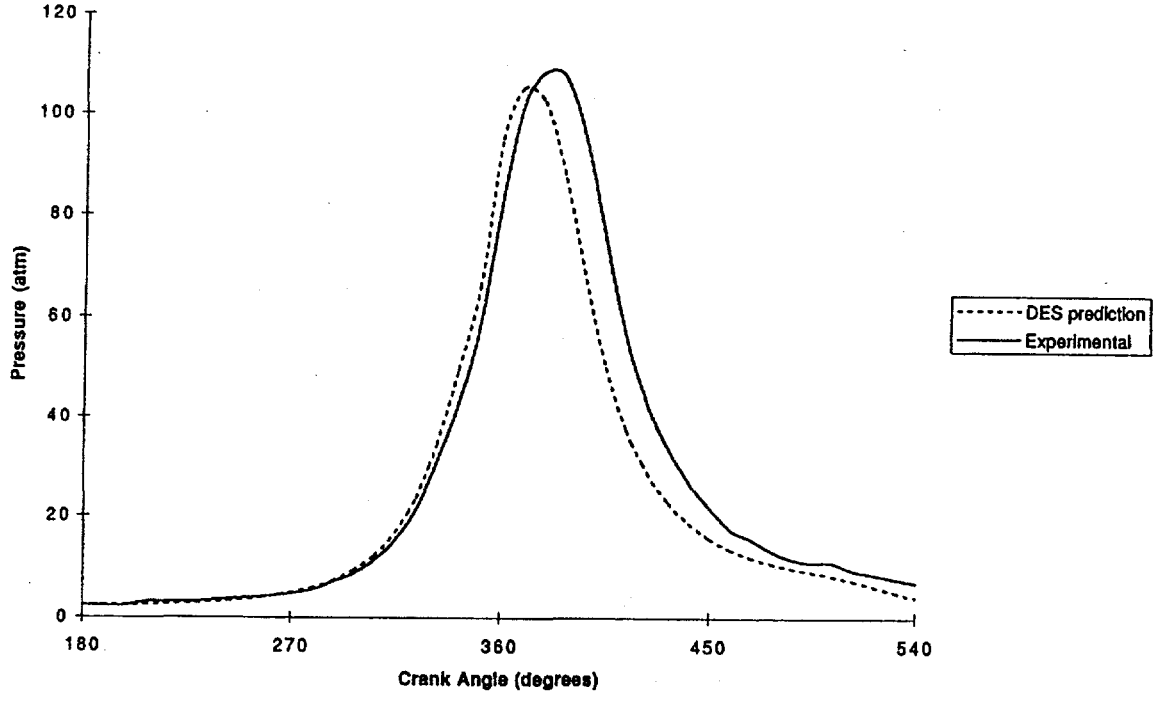

FIGURE 4.2 Predicted and Measured Cylinder-Pressure Profiles

4.2.2 Model Matching with New Heat-Release Correlation

The diesel engine model was calibrated through tuning of its adjustable constants related to the computation of the discharge and heat transfer coefficients, as well as overall friction, for operation at Notch 8 (full load) with standard air. The frictional losses were estimated on the basis of the Millington and Hartles correlation (1968). The heat-release correlation of Equation 2-11 was used; the values assumed for the adjustable constants were those predicted by Equation 2-12 for 21% oxygen content. After air flow and other available brake quantities were matched within 2% at notch 8, the ability of the simulation to predict performance at six other notch positions (without any further tuning) was explored. Measured data for the GE engine at the various notch positions included such input parameters as engine speed, mass of fuel injected, intake and exhaust temperature and pressure, and volumetric efficiency. Output parameters included brake power, brake-specific fuel consumption (bsfc), brake mean effective pressure (bmep), air mass flow, air/fuel ratio, and brake thermal efficiency.

Figure 4.3 compares predicted brake power, bsfc, bmep, and air mass flow rate with corresponding measurements at six notch positions. Over the range of notch positions examined, the diesel engine simulation underpredicted brake power, bmep, and air flow by about 2 to 7%, while it correspondingly overpredicted bsfc by about 2 to 7%. Although agreement between baseline engine predictions and data could be improved by further tuning the model constants, it was felt that such an exercise was not warranted. First, a complete and reliable experimental database at all notch positions (specifically, pressure and heat-release rate) was not available when the diesel engine simulation was being matched to the engine. Second, the present study is intended to assess relative performance changes when the intake air for the engine is supplied with various oxygen levels, not to focus on baseline engine performance predictions.

4.3 Engine Gross Performance under Various Oxygen-Enrichment Levels

A constant oxygen-to-fuel ratio was used as the basis to compare engine performance under different levels of oxygen enrichment in the intake air. The mass of fuel injected per cylinder per cycle was increased proportionally to the oxygen level in the intake air to maintain a constant oxygen-to-fuel ratio. The gross brake power, bsfc, bmep, and peak cylinder pressure obtained when oxygen levels ranged from 21 to 35% (by volume) are shown in Figure 4.4 for all six notch positions. The amounts of power that would be required by the membrane to supply the desired intake air oxygen concentrations are not captured in the gross performance estimates but are accounted for in a subsequent section to arrive at net performance improvements. The model predictions indicate that cylinder brake power significantly increases when the intake air oxygen concentration increases from 21 to 35%. A substantial (10%) output improvement can be achieved as the result of a relatively small increase in oxygen content, to 23% by volume, while up to 90% improvements can be achieved when the oxygen content is increased to 35%. When the intake oxygen content was increased from 23 to 35%, the cylinder brake output increased from about 10 to 90% at notch positions 8 through 5. At lower notch positions (4 and 3), the

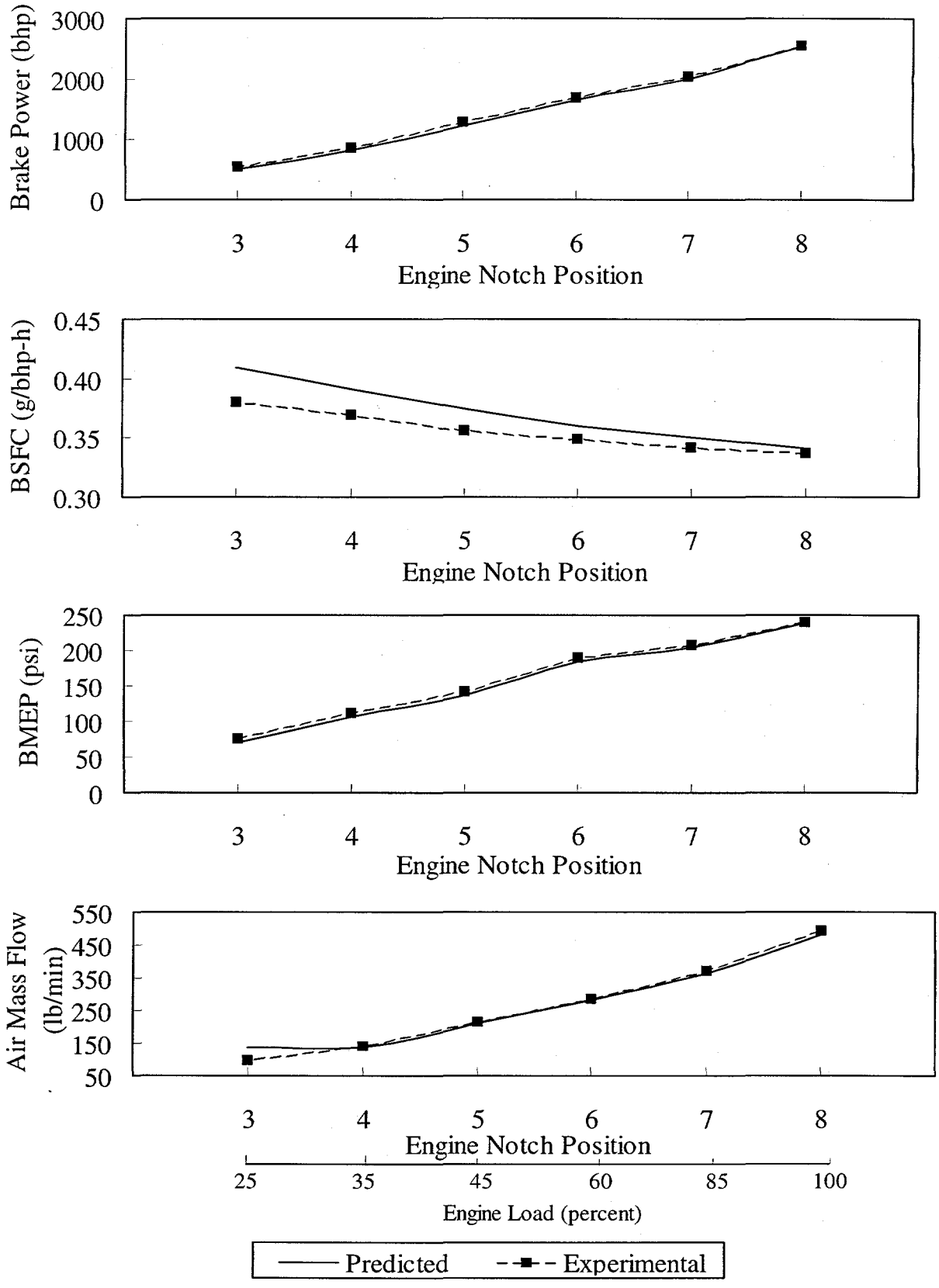

FIGURE 4.3 Validation of Diesel Simulation with Experimental Results

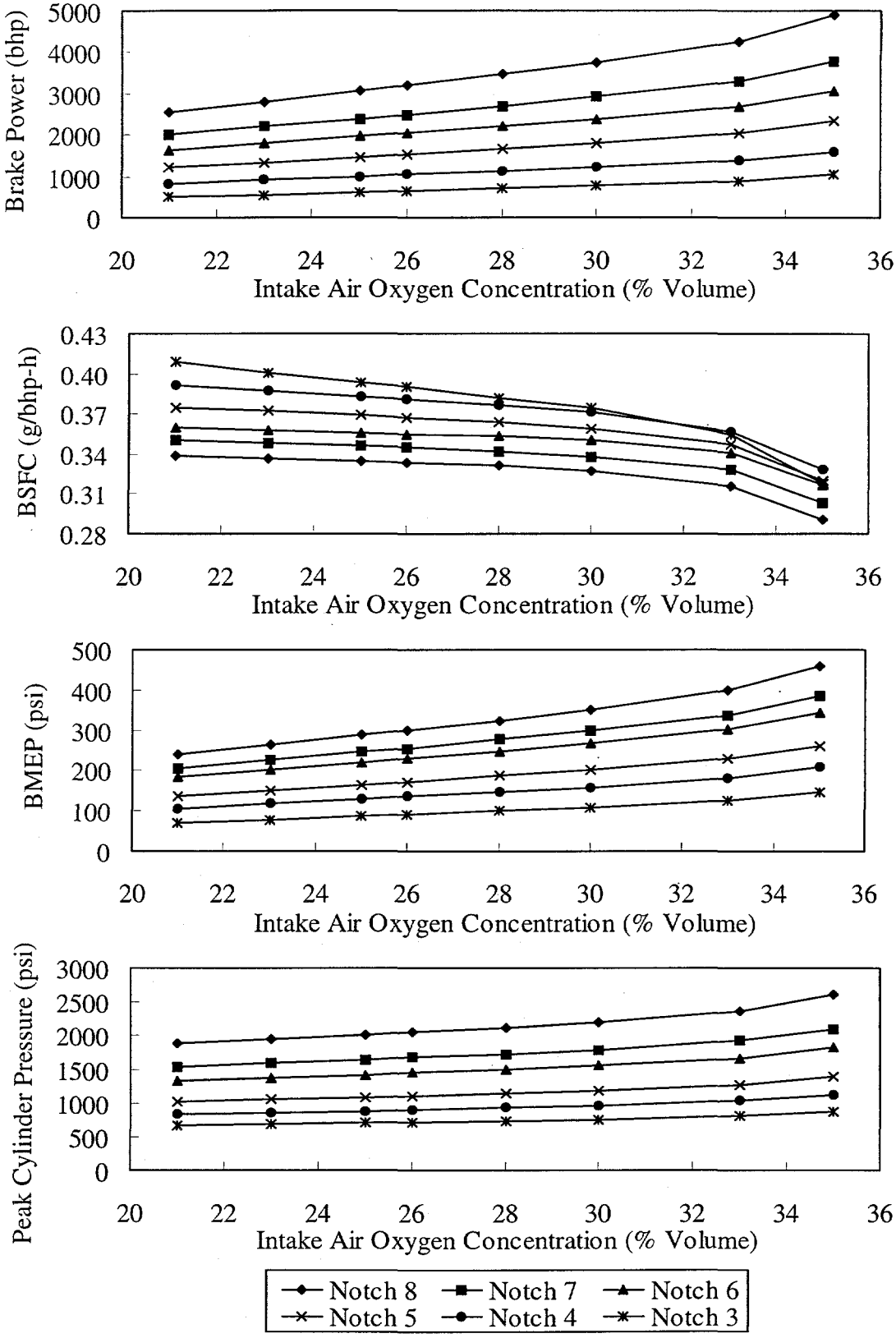

FIGURE 4.4 Effects of Intake Air Oxygen Enrichment on Engine Performance at Various Notch Positions

cylinder output increased even more, by approximately 12 and 110% at oxygen-enrichment levels of 23 and 35%, respectively. The enhanced power output resulting from oxygen enrichment was accompanied by higher bmep and lower bsfc. At notch 8, the bsfc decreased from 0.339 to 0.29 g/bhp-h (about 15% reduction) when the intake air oxygen level was increased from 21 to 35%. A similar reduction in bsfc was observed at other notch positions, more predominantly at lower notch positions (4 and 3). The implied thermal efficiency improvements are attributed to faster burn rates, particularly during the diffusion phase of combustion (Assanis et al. 1990; Sekar et al. 1991a). Despite the advantages of lower bsfc, higher cylinder output, and higher bmep, the peak cylinder pressures were higher by about 3 and 35% when the intake air oxygen level was increased to 23% and 35%, respectively, over ambient air. However, the increase in peak cylinder pressure was smaller than the increase in cylinder output. This feature of the oxygen-enriched engine is attractive, particularly because some of the other techniques for increasing power output (increased compression ratio, high boost turbocharging) typically yield power improvements proportional to peak pressure increases.

4.4 Effects of Fuel Injection Timing with Oxygen Enrichment

Oxygen-enriched combustion leads to shorter ignition delays, higher diffusion burn rates, and faster completion of the combustion process (Sekar et al. 1991a). These effects should permit the fuel injection timing to be retarded to contain the peak cylinder pressure within a specified ceiling while still allowing some of the performance benefits resulting from oxygen enrichment to be realized. Retarded fuel injection timing should also help to lower combustion temperatures and NO formation levels associated with oxygen enrichment.

Figure 4.5 shows the effects of fuel injection timing on the performance characteristics of an engine operating at full load (notch 8) with intake air at various oxygen-enrichment levels (23 to 30% by volume). The deterioration in brake power, bsfc, and bmep that resulted from retarding the fuel injection timing by four crank angle (CA) degrees was marginal (<1%) compared with the decrease in peak cylinder pressure (about 7%). Retarding the injection timing further (up to 12 CA degrees), combined with oxygen enrichment, resulted in a reduction in the engine power output and bmep of about 4% and an increase in bsfc of about 4%. However, the corresponding peak cylinder pressure decreased by approximately 22%, almost uniformly within the range of oxygen contents examined. The additional oxygen available in the combustion air shortened the ignition delay of the fuel-air mixture, and thus, the magnitude of the premixed heat release (as captured by the heat-release correlation). In addition, the faster diffusion burn rates still allowed combustion to proceed in an optimal manner, so it reached its peak within 10 to 16 CA degrees after TDC for the optimal retarding of timing. Figure 4.6 shows an injection timing map that indicates the relationship between brake power and peak cylinder pressure for various oxygen levels in the intake air. With the fuel injection timing retarded by between 4 and 8 CA degrees for the various oxygen-enrichment levels, the peak cylinder pressure can be brought down to that achieved when standard air is used. The corresponding decrease in brake power and increase in bsfc at any particular oxygen-enrichment level was only about 3%. For example, at a constant peak cylinder pressure (like that of the base engine), the cylinder brake output increased by about 45% when the intake air oxygen level was increased from 21 to 30% and the fuel injection timing was retarded by about 8 CA degrees. The higher cylinder brake

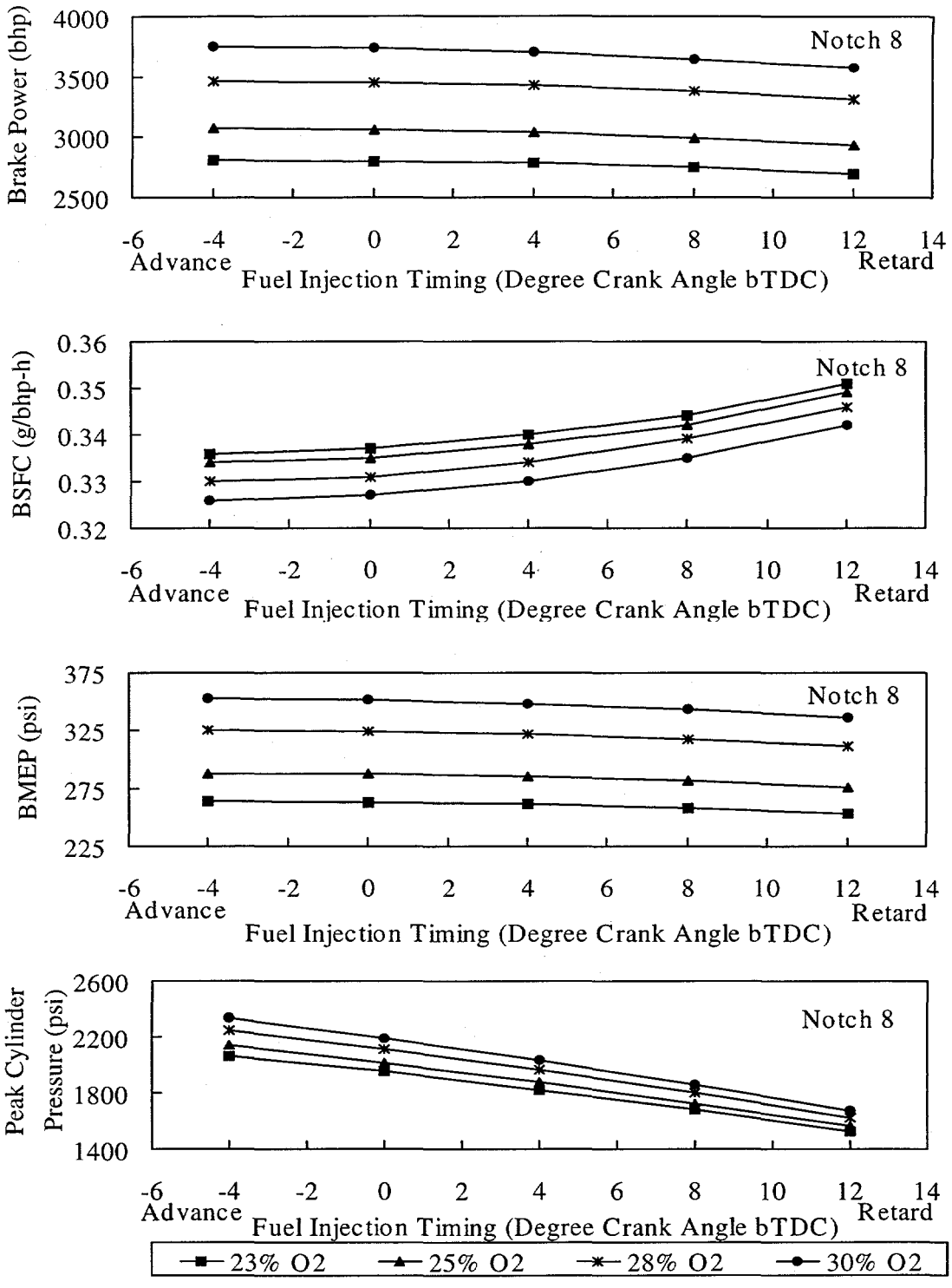

FIGURE 4.5 Effects of Fuel Injection Timing on Performance Characteristics

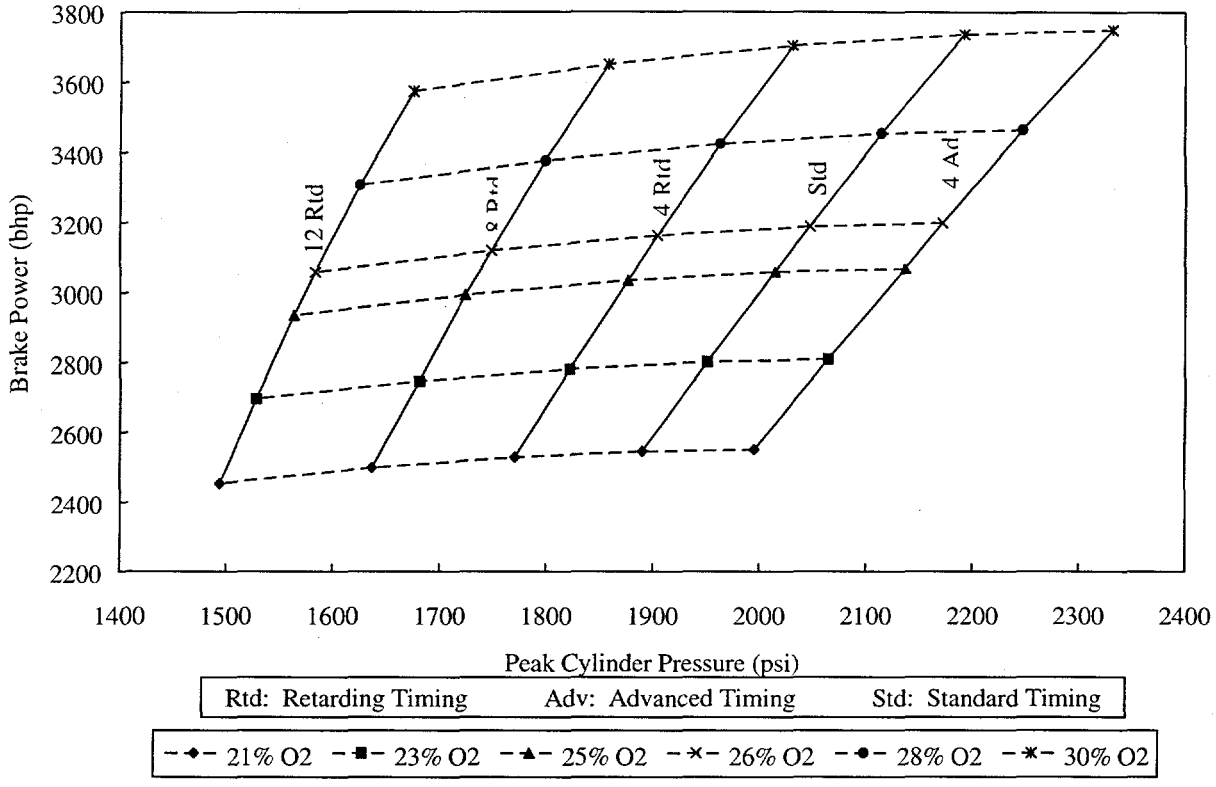

FIGURE 4.6 Fuel Injection Timing Map: Brake Power vs Peak Cylinder Pressure at Various Intake Air Oxygen-Enrichment Levels

output at the same or a marginally high peak cylinder pressure is clearly one advantage of oxygen-enriched combusion over other methods of increasing the power output from a given engine displacement.

4.5 NO Emissions

Higher post-flame temperatures and oxygen concentrations during the combustion process result in higher NO formation rates (Heywood 1988). For a given combustion chamber, NO emissions correlate with variations in the stoichiometric flame temperature, which is dependent on inlet pressure and temperature and the chemical composition of the fuel and oxidant (Plee et al. 1982). In the present work, variations in the stoichiometric, adiabatic flame temperature with changes in the oxygen concentration in the combustion air were studied by keeping all other influencing parameters (inlet pressure, temperature, and fuel composition) constant. The instantaneous traces of adiabatic flame temperature and overall, bulk gas temperature when 21% and 26% oxygen concentrations were used are depicted in Figure 4.7. When the intake oxygen concentration was increased from 21 to 26% (by volume), the peak stoichiometric flame temperatures and the gas temperatures rose by about 240 K. This result can be readily explained; the extra number of oxygen molecules in oxygen-enriched combustion displace nonreacting nitrogen molecules, which normally act as a diluent and cool down the

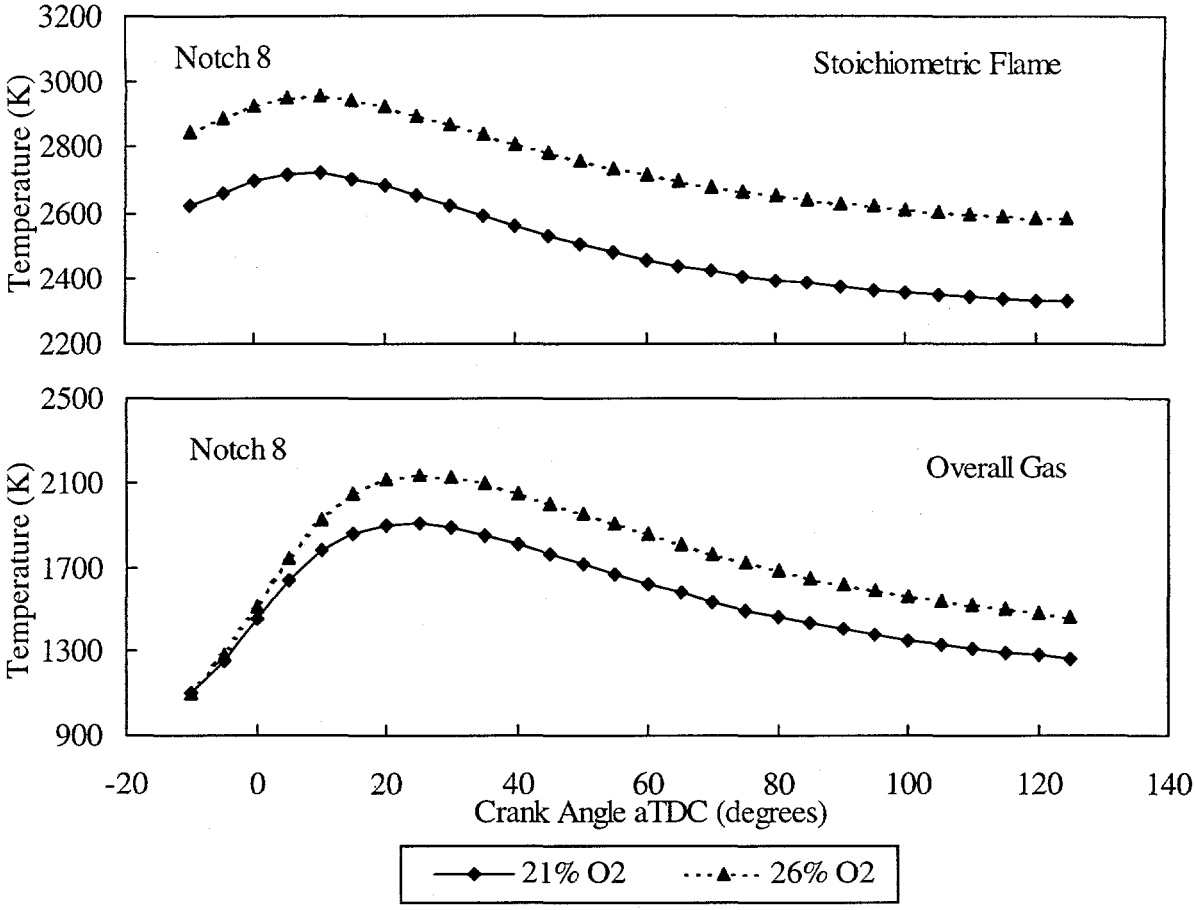

FIGURE 4.7 Overall Combustion and Stoichiometric Core-Flame Temperatures with Intake Air Oxygen Enrichment

flame. This result corroborates the correlation of adiabatic flame temperature with intake air effects, as established by several other researchers (Sawyer et al. 1973; Plee et al. 1982).

The NO formation histories during the combustion period are shown in Figure 4.8 for both ambient air and 26% oxygen-enriched intake air. Instantaneous NO concentrations are shown as a fraction of the contents in the burned core zone and the overall cylinder. The instantaneous NO concentrations were considerably higher with 26% oxygen-enriched intake air than with standard air. As combustion temperatures dropped, the NO concentrations froze at concentrations higher than equilibrium at the given temperature and pressure. The cycle-integrated NO concentrations (as a fraction of the adiabatic burned gas and the overall gas) are shown in Figure 4.9 for various oxygen-enrichment levels. Evidently, the NO emissions increased significantly when the intake air oxygen concentrations were increased. For instance, when the intake oxygen was increased from 21 to 26%, the cylinder-out NO emissions increased by about 2,100 parts per million (ppm). During operation at 30% oxygen content, the NO emissions increased by a factor of three, from 1,600 to 5,000 ppm. This increase in NO concentration corroborates previously published results on the effects of oxygen enrichment on NO emissions (Ghojel et al. 1983; Iida and Sato 1988).

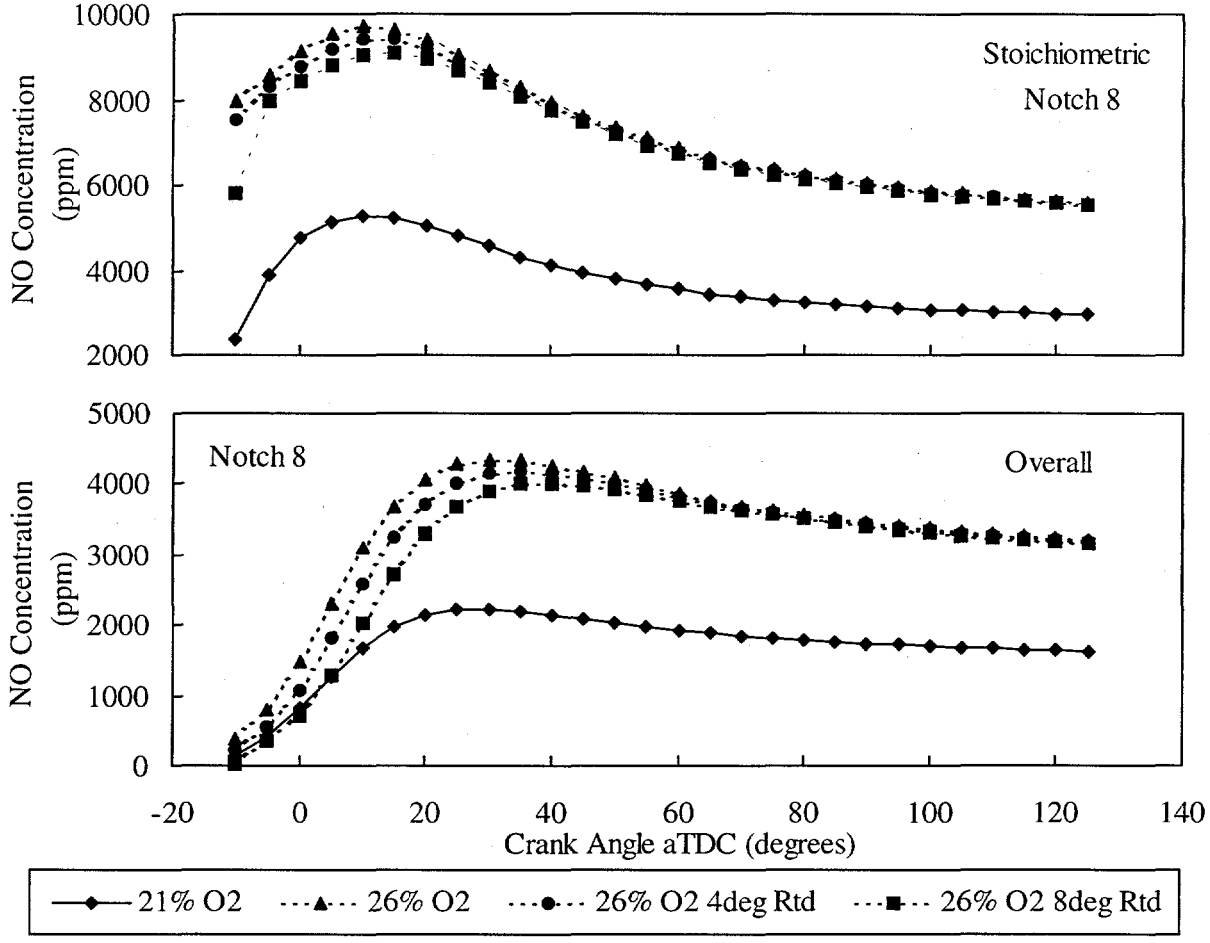

FIGURE 4.8 Effects of Oxygen and Injection Timing on NO Emissions in Stoichiometric and Overall Combustion Regions

Higher NO emissions, which are concomitant with higher combustion temperatures, are one of the major drawbacks of oxygen-enrichment technology. As a possible remedy, fuel injection timing was varied to determine whether it could influence the NO formation associated with oxygen enrichment. When the injection timing was retarded, the peak cylinder pressure and maximum overall in-cylinder gas temperatures decreased. However, computations showed that engine-out NO emissions decreased by only 50 to 100 ppm when fuel injection timing was retarded 4 to 12 CA degrees and oxygen-enriched intake air was used. Clearly, the NO emission reductions obtained as a result of retarding fuel injection timing were marginal compared with the NO emission increases obtained when the oxygen concentration was increased from 21 to 26%. This result can be attributed to the fact that retarding injection timing does little to affect flame temperature, which is predominantly affected by increased oxygen concentration in the air. It appears that other control technologies are needed to overcome the NO penalty associated with oxygen enrichment. Some methods that have been explored to keep NO levels reasonably low when oxygen-enriched intake air is used include adding water in either the intake air or the fuel (Assanis et al. 1990) and using monatomic nitrogen, induced by a pulsed arc, as a post-treatment device (Ng et al. 1995).

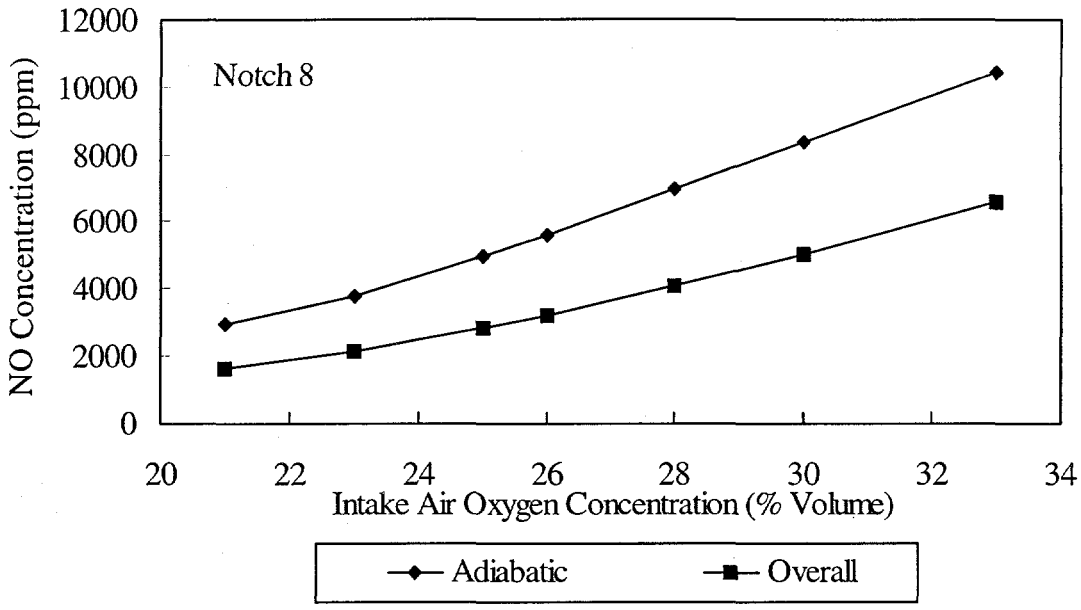

FIGURE 4.9 Nitric Oxide Concentrations at Different Intake Air Oxygen-Enrichment Levels

4.6 Membrane Size and Power Requirements

An estimate of the power required by the membrane to supply the desired level of oxygen enrichment is necessary to assess the net power improvement obtained from an engine operating with oxygen-enriched intake air. The simplified membrane model was used to compute the membrane power and size required for an engine operating at full load and different intake air oxygen-enrichment levels. The predicted variation in permeate oxygen concentration with stage cut at various feed-to-permeate pressure ratios is shown in Figure 4.10 for two CMS membrane materials. Between the two CMS materials (CMS-3 and CMS-7), CMS-3 gave higher stage cuts at a given permeate oxygen and at a specified pressure ratio between the feed and permeate. This was mainly because of the higher selectivity associated with the CMS-3 material. To obtain high stage cut and high purity, both selectivity and permeability should be high; these properties are difficult to achieve because of the inherent tradeoffs between membrane permeability and selectivity. Data on the feed flow rate, permeate flow rate, and pressure ratios across the module were used to obtain the membrane power data. The total isentropic work required to drive the membrane module to produce the desired oxygen concentration and the permeate flow rate under the three alternative operating modes are shown in Figure 4.11. The pressure mode is clearly the most power-intensive because the pumping work is done on the feed air. On the other hand, the mixed mode requires the least power for moderate levels (up to 26%) of permeate oxygen. At higher permeate oxygen levels, the vacuum mode requires less power than the other two modes, mainly because the purity of the oxygen concentration of the mixing stream is limited to

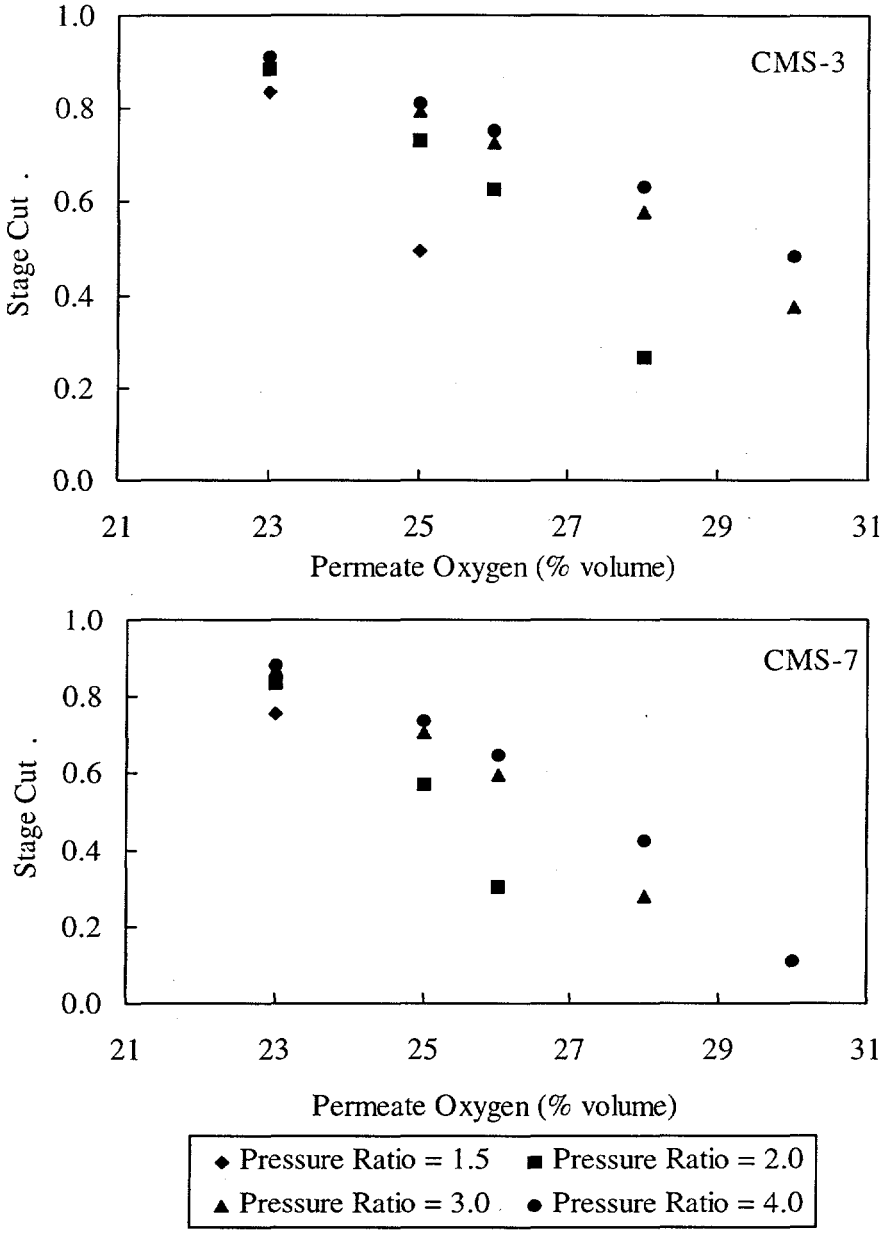

FIGURE 4.10 Variation of Permeate Oxygen Concentration with Stage Cut at Various Pressure Ratios for CMS Membrane Materials

30% or less (by volume) when either CMS-3 or CMS-7 membrane material is used. The selection of a preferred mode of operation depends on the economic tradeoffs among membrane area costs, auxiliary equipment costs, input power requirements (to maintain required pressure/vacuum), and system compactness. The minimum isentropic work required to yield a prescribed level of permeate oxygen under full-load engine operation (Notch 8) is shown in Figure 4.12 for both CMS materials. CMS-3 requires less power because its selectivity and stage cut are relatively higher than those of CMS-7.

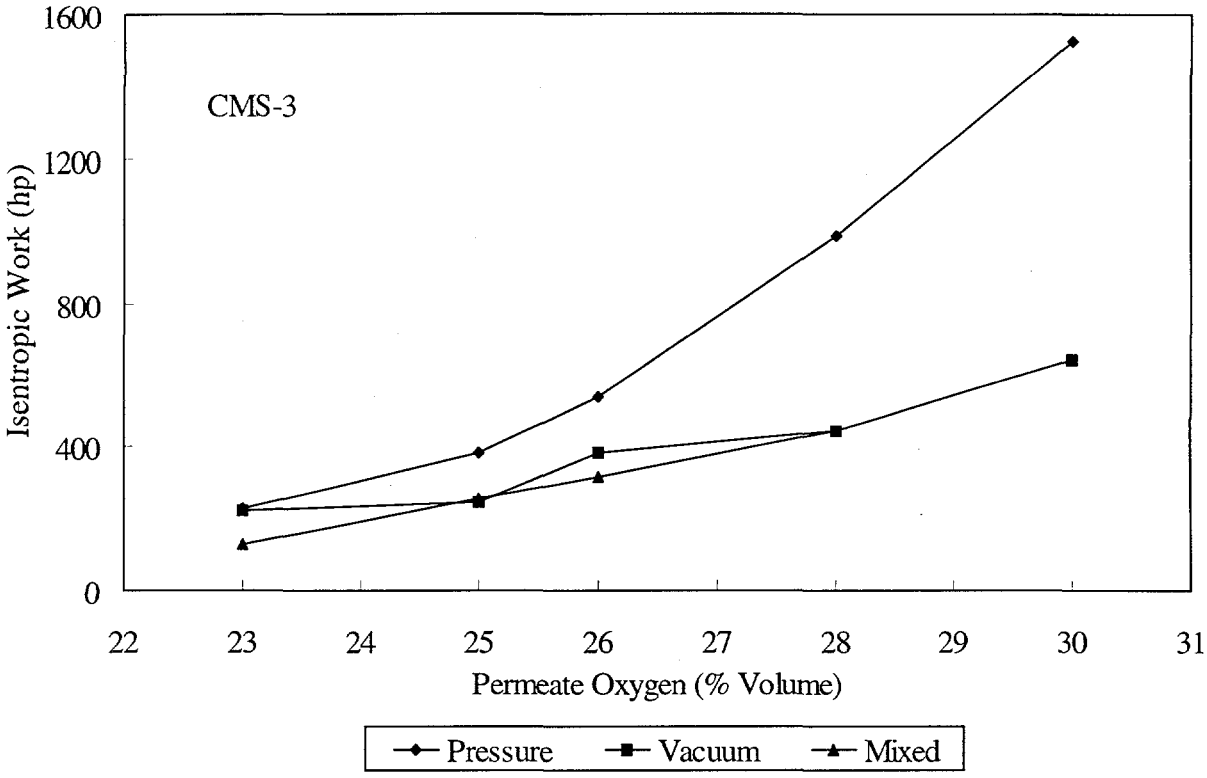

FIGURE 4.11 Total Isentropic Work Required by Membrane under Three Operating Modes

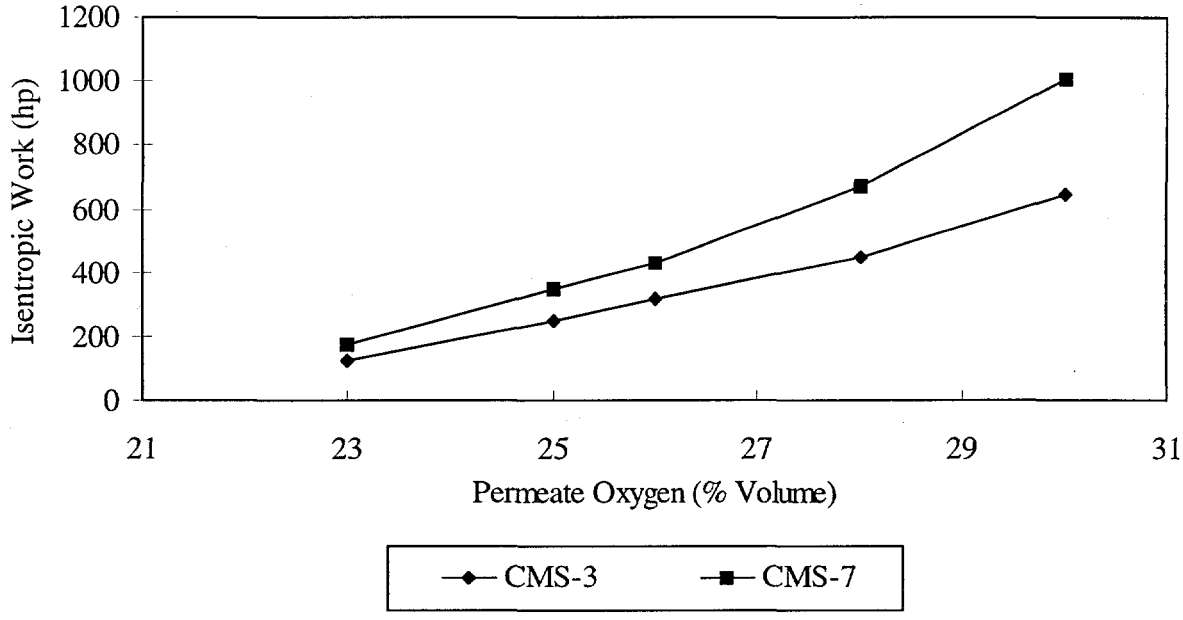

FIGURE 4.12 Minimum Isentropic Work Required by Membrane Modules at Various Oxygen-Enrichment Levels

TABLE 4.3 Design Estimates of Membrane Size and Power Requirements for Two Different Materials Operating in Mixed Mode to Supply 26% Oxygen in the Intake Air at Full Load

Material	Membrane Surface Area (10^3 ft^2)	Active Fiber Length (ft)	No. of Fibers (10^3)	Module Volume (ft^3)	Approximate Cylindrical Module Dimensions, L x D (ft)	Membrane Isentropic Work (bhp)
CMS-3	23.68	3	1,532	37	3 x 4	318
		4	1,150	28	4 x 3	
CMS-7	8.13	3	527	12.7	3 x 2.3	431
		4	395	9.5	4 x 1.7	

Table 4.3 compares some membrane performance parameters, including surface area, module volume, and isentropic work, required to supply 26% oxygen-enriched air to a locomotive engine operating at full load. The CMS-3 module occupied more space but required less power than the CMS-7 module. The tradeoff between membrane size and power is apparent. This tradeoff is inherent in membranes because of their intrinsic properties (permeability versus selectivity). For example, CMS-3 has a relatively low permeability but high selectivity, and thus requires less power but a larger module size. Conversely, CMS-7 has a relatively high permeability but low selectivity, and thus requires more power but a smaller module size. The tradeoffs among membrane properties and operating modes suggest that a detailed optimization study should be conducted to arrive at the smallest possible size and lowest amount of power required for any given application.

4.7 Engine Performance with Membrane Supplying Oxygen-Enriched Air

The work required by an air separator membrane to supply the desired oxygen concentration in the engine intake air has to be considered to evaluate the net brake output obtained from the engine. Computation of the parasitic power requirements of an air separator module involves optimizing several physical and operating characteristics of the membrane. Because design information is limited and there is no detailed membrane model, the accuracy of estimating membrane power requirements is compromised. However, for the preliminary membrane design arrived at in the previous section, membrane power requirements were estimated as a function of the permeate oxygen level for two candidate materials (Figure 4.12). On the assumption that an air separator module made of CMS-3 membrane material and operating under the mixed mode supplies the desired oxygen concentration in the intake air, the net brake power output (cylinder brake power minus membrane work) was computed at full load, as shown in Figure 4.13. On the basis of the present membrane model, the net engine power improvements were found to be about 4 and 15% when the intake air oxygen was increased to 23 and 30%, respectively. Evidently, the net brake power improvements obtained from the engine that used oxygen-enriched intake air were considerably smaller than the gross cylinder output (without allowing for membrane work). Any reduction in membrane power requirements would

directly enhance the net power improvements. However, for a detailed design and ultimate assessment of the membrane potential, more accurate computations of membrane power requirements should be carried out, taking into consideration all tradeoffs among membrane intrinsic properties and operating conditions.

4.8 Oxygen Enrichment vs Turbocharging

Turbocharging is a proven, practical method to obtain a higher power output than the natural aspiration from a given engine displacement. However, there are practical limits to boosting intake manifold pressure before the complexity and losses associated with compressing the air are increased considerably (e.g., need for two-stage turbocharging and intercooling). Use of oxygen-enriched intake air can be considered as an alternative or as a complementary method to boost the power output. In the present work, an attempt was made to quantify the difference between highly boosted turbocharging vs oxygen enrichment plus regular boost, in terms of the brake power obtainable at any specified peak cylinder pressure.

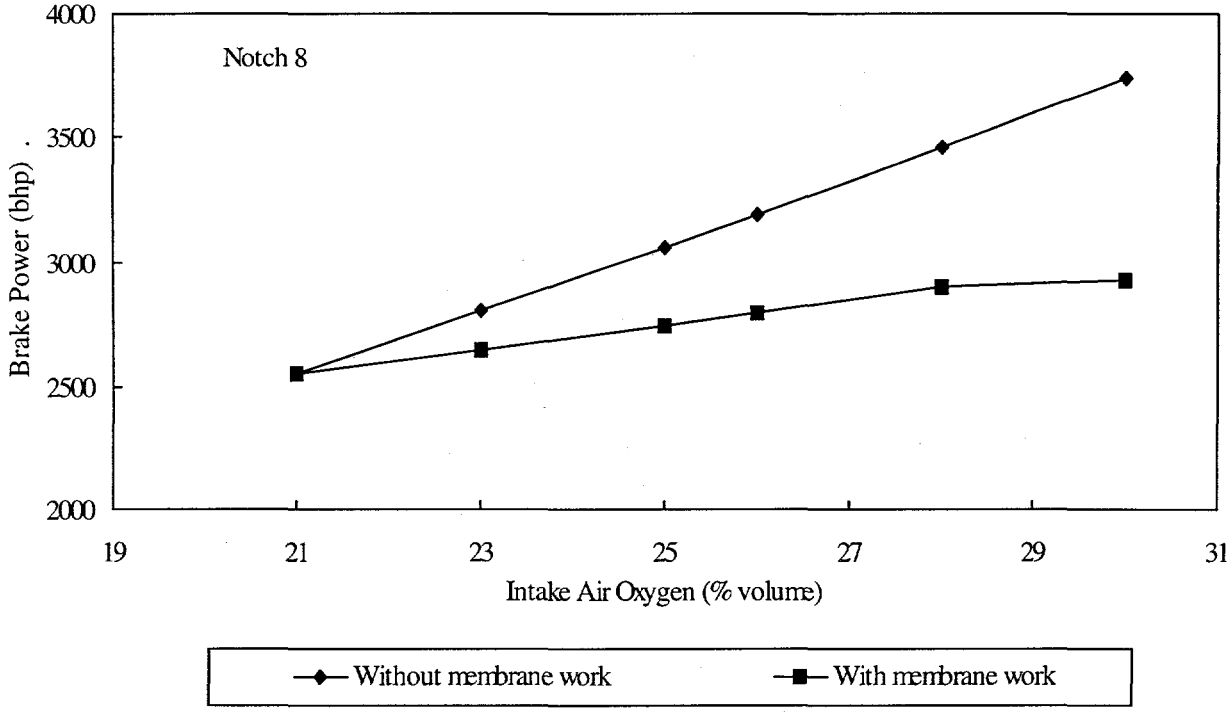

FIGURE 4.13 Potential of Brake Power Enhancement with Oxygen Enrichment at Full Load

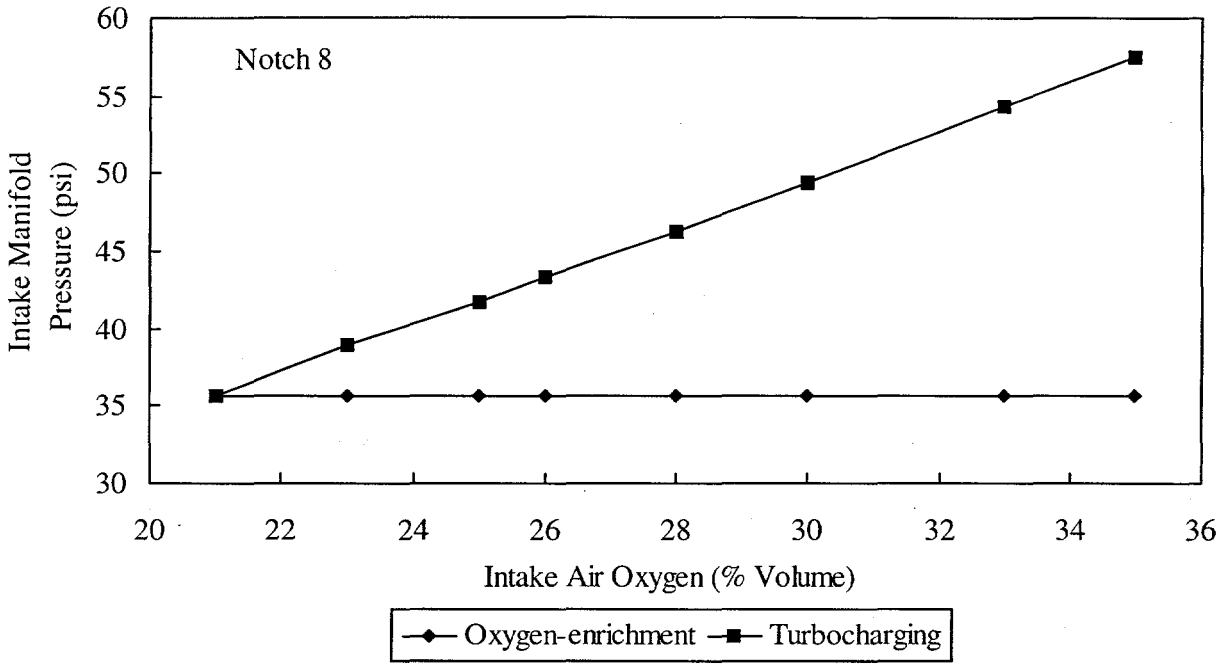

FIGURE 4.14 Intake Manifold Pressure with High-Boost Turbocharging Corresponding to Various Intake Air Oxygen-Enrichment Levels

To admit the same mass of oxygen per cycle as that occurring with oxygen enrichment, turbocharging requires a considerably higher intake manifold pressure. Figure 4.14 illustrates the required increase in intake manifold pressure with turbocharging so as to admit the same mass of oxygen per cycle as with oxygen enrichment. At full load, turbocharging requires the intake manifold pressure to be increased from 35 to 57 psi as the oxygen content is increased from 21 to 35% by volume in the intake air. The same mass of fuel is injected in both cases, so that they operate with the same oxygen-to-fuel ratio. The considerably increased compression work resulting from the highly boosted air and its extra mass of nitrogen are reduced in the case of oxygen enrichment. As a result, the gross cylinder power obtained is considerably higher with oxygen enrichment than with high-boost turbocharging at any constant peak cylinder pressure (see Figure 4.15). When the membrane power is subtracted from the cylinder output, the difference between oxygen enrichment and turbocharging appears to be minimal for operation at the base injection timing (Figure 4.15). However, an oxygen-enriched engine, with its shorter delay and faster diffusion burn period, can operate with an injection timing that is retarded so that peak cylinder pressure is reduced, as discussed previously. When this strategy is followed, the net brake power obtainable at any constant peak cylinder pressure is higher with oxygen enrichment than with high-boost turbocharging. For instance, by using 28% oxygen concentration and fuel injection timing retarded by 4 CA degrees, a 4% increase in peak cylinder pressure could result in an increase in engine net power of approximately 13%, compared with an increase of only 4% by using turbocharging. In general, power enhancement with increased turbocharging is fairly proportional to the increase in peak cylinder pressure, whereas the benefit is almost doubled with oxygen enrichment.

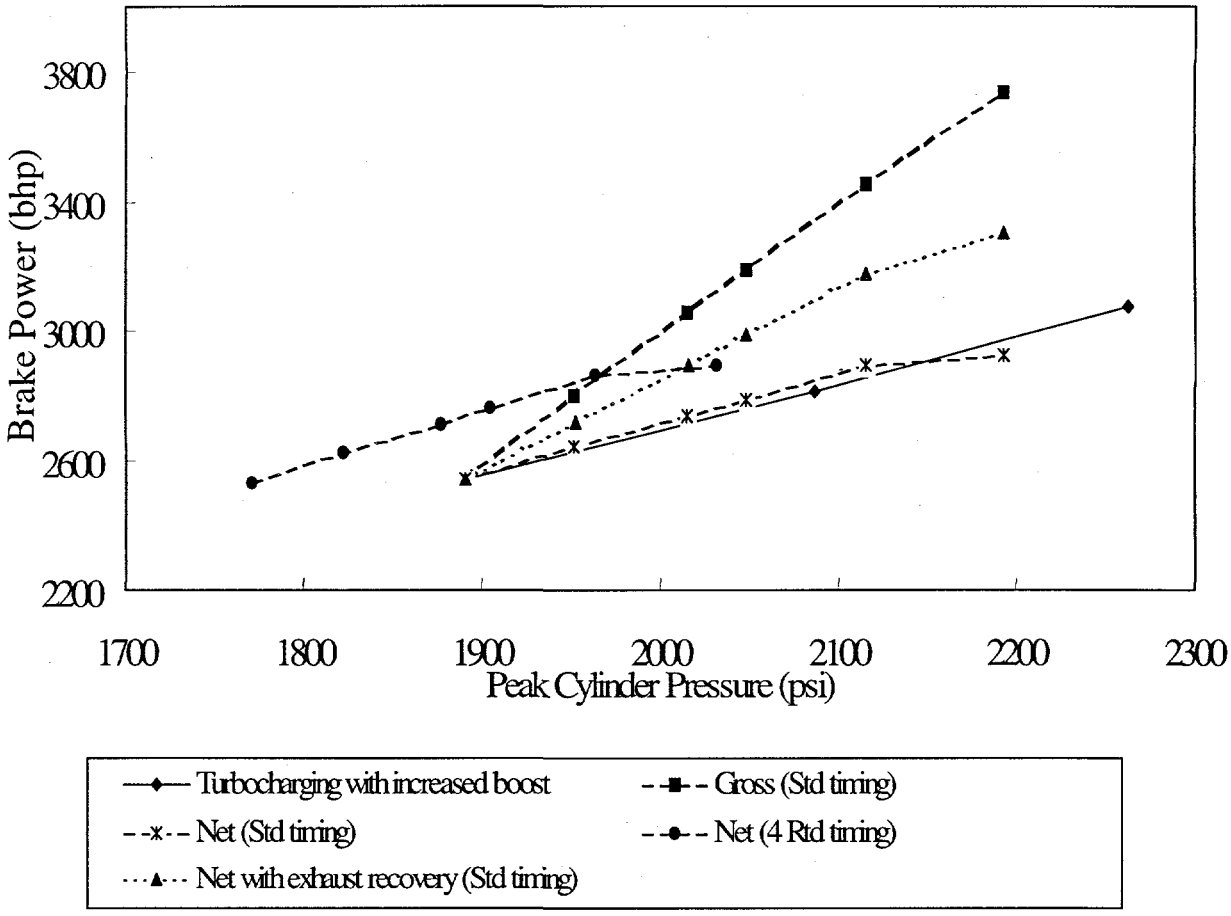

FIGURE 4.15 Potential of Oxygen Enrichment over Turbocharging with Increased Boost to Enhance Power Output

Figure 4.16 compares the turbine exit temperatures for operation with highly-boosted turbocharging and oxygen enrichment under standard fuel injection timing. At a constant oxygen-to-fuel ratio, exhaust gas temperatures at the turbine exit were considerably higher (100 to 500 K) with oxygen enrichment than with turbocharging because of the higher flame temperatures of the former. If part of the additional exhaust energy that is available with oxygen enrichment were recovered, the net power improvement of the oxygen-enriched engine would be more attractive. To quantify the expected improvement, the difference in exhaust enthalpy past the turbine under operation with oxygen enrichment vs increased inlet boost turbocharging was assumed to be recovered by using an organic Rankine cycle with 20% overall thermal efficiency. The additional power obtained from the recovered exhaust energy was then added to the net brake power of the oxygen-enriched engine, as shown in Figure 4.15. For a 12% increase in peak cylinder pressure, the net power obtained by using oxygen-enriched air with exhaust recovery increased from 14 to 25%, whereas the power improvement that resulted from using an increased inlet boost was only 13%. Hence, it is essential to recover part of the incremental exhaust energy with oxygen enrichment so that the net power improvements from a given engine are competitive with other conventional methods.

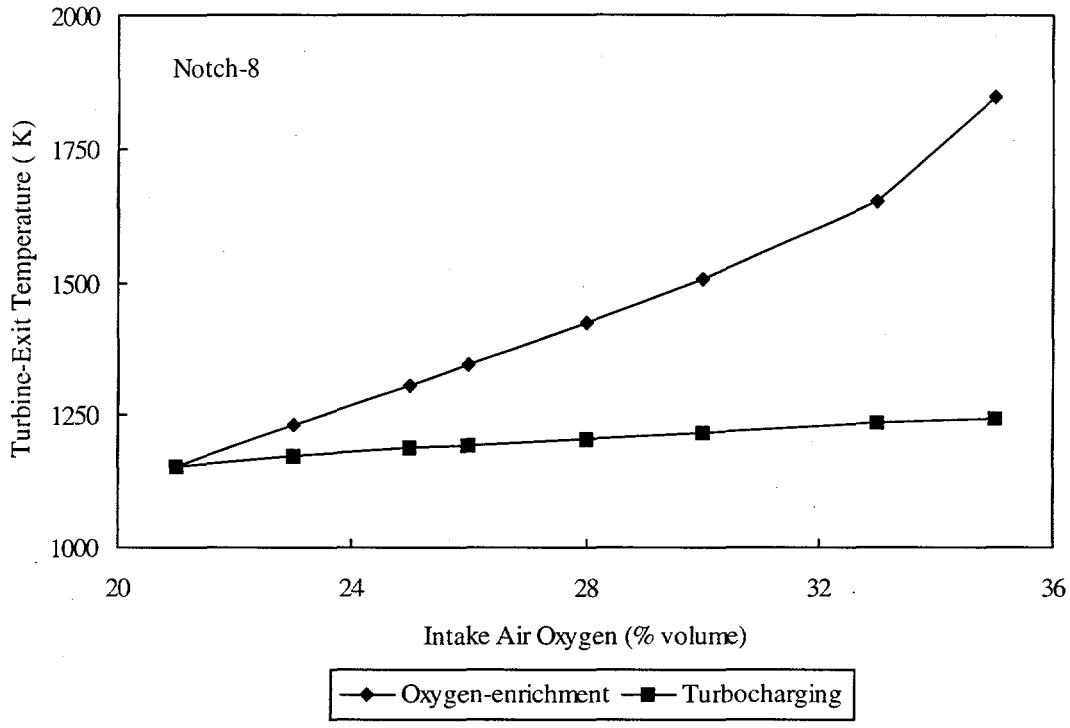

FIGURE 4.16 Turbine-Exit Temperatures for Both High-Boost Turbocharging and Oxygen Enrichment at Constant Oxygen-to-Fuel Ratio

5 Economic Analysis

5.1 Introduction

The economic feasibility of oxygen-enrichment technology for locomotive diesel engines was analyzed. The base case engine parameters and assumptions associated with the spreadsheet model were presented. On the basis of mixed-mode operation of an air separation membrane system, the required auxiliary equipment for supplying oxygen-enriched intake air for the diesel engine was determined, sized for capacity, and priced. Replacement analyses that used three types of capital budgeting techniques involving annual cash flow analysis were done for a 26% oxygen-enrichment level, with and without exhaust energy recovery. The results of the financial analysis are presented and discussed.

5.2 Oxygen-Enrichment Systems Determination

The basis for the cost analysis was an oxygen-enrichment system operating in mixed mode to supply 26% oxygen-enriched combustion air for a locomotive diesel engine operating at its full load. As indicated in Section 4.6, it was clear that the membrane power requirements were the lowest with mixed-mode operation compared with the pressure and vacuum modes of operation. Lower membrane parasitic losses allow higher net power to be obtained from a given engine, which is the most desirable operation from an economic point of view. Hence, the vacuum and pressure modes of operation were not considered in this analysis. The operating conditions of the air separation membrane and specifications of the auxiliary equipment for 26% oxygen-enrichment are presented in Table 5.1. The required equipment (a blower to supply positive air flow in the feed stream and a vacuum pump to maintain the desired vacuum at the permeate stream, to attain the required oxygen-enrichment level) for the oxygen-enrichment system (operating in mixed mode) was sized, and various vendors were contacted to obtain performance and pricing information. Two different types of membrane materials, CMS-3 and CMS-7, were considered for the oxygen-enrichment system. The projected membrane cost ($3 per square foot of surface area) was obtained from the membrane manufacturer (Nemser 1996). The "ballpark" estimates of blowers and vacuum pumps were obtained from Cocharne Compressor Company (Gary 1996). The membrane and auxiliary equipment costs of the oxygen-enrichment system for two different membrane materials are also presented in Table 5.1. For cost analysis, the required oxygen concentration in the engine intake air operating at its full load is considered to be 26% by volume. In the absence of several membrane and auxiliary equipment cost data, the economic benefits of using oxygen enrichment at other oxygen concentrations were not studied.

On the basis of constant oxygen-to-fuel ratio and constant volumetric efficiency, gross power and fuel consumption data were obtained from the results of diesel simulation studies (see Section 4.3) for both the base engine and an engine supplied with oxygen-enriched intake air, respectively. It was clear from the results that the engine supplied with oxygen-enriched

TABLE 5.1 Oxygen-Enrichment System Costs for Two Different Membrane Materials

Item	Membrane Material	
	CMS-3	CMS-7
Membrane Device		
Combustion air oxygen concentration, by volume (%)	26	26
Mode of operation	Mixed	Mixed
Engine intake air flow (acfm)	7,016	7,016
Oxygen concentration at permeate, by volume (%)	28	26
Percent permeate added to main flow	71.40	100
Stage cut	0.575	0.305
Feed pressure (psia)	15	15
Permeate pressure (psi)	7.5	7.5
Pressure ratio between feed and permeate	2	2
Retentate pressure (psia)	14.9	14.9
Membrane surface area (ft^2)	23,680	8,130
Membrane cost (@\$3/ft^2)	\$71,040	\$24,390
Membrane casing (10% of membrane)	\$7,104	\$2,439
Total membrane cost	\$78,144	\$26,829
Auxiliary Equipment		
Blower flow (acfm)	8,700	23,000
Ideal work (hp)	78	94.7
Efficiency (%)	80	80
Actual work (bhp)	97.5	118.4
Blower cost	\$65,000	\$95,000
Vacuum pump flow (acfm)	5,000	7,016
Ideal work (hp)	240.4	295.6
Efficiency (%)	70	70
Actual work (bhp)	343.4	422.2
Vacuum pump cost	\$62,000	\$77,500
Total auxiliary equipment cost	\$127,000	\$172,500
Hardware and Controls (20% of auxiliary equipment)	\$25,400	\$34,500
Total Cost of Oxygen-Enrichment System	\$230,544	\$233,829

combustion air will consume more fuel and hence produce more power. Therefore, the net power that can be obtained from the engine would be the difference between gross power and membrane parasitic power requirements. Capital cost of the standard 12-cylinder locomotive diesel engine was assumed to be \$300/bhp. Oxygen-enrichment levels up to 26% by volume resulted in only a marginal increase in the peak cylinder pressure (see Sections 4.3 and 4.6). Hence, we assumed that the modifications required on the base engine to accommodate the

increase in peak cylinder pressures with oxygen-enrichment were neglected. The economic advantage of recovering a part of the exhaust gas energy was illustrated. In this case, the net power obtained from the engine was simply added to the engine brake power after subtracting the membrane power requirements. With more net power produced from the same engine capacity, the sale price of the engine would be higher. We assumed that the increase in sale price was at the rate of $300/bhp. Hence, the gain in engine capital was computed on the basis of the difference in net power obtained with respect to the base engine. In the absence of organic Rankine cycle equipment cost for recovering the exhaust energy, the required equipment and control costs were estimated at the rate of $500 per bhp from the recovered exhaust energy. The differential capital investment was obtained from the oxygen-enrichment system cost, exhaust energy recovery system, and gain in engine capital due to increased net power. Table 5.2 shows various capital costs associated with engine power, with two different membrane systems supplying 26% oxygen-enriched combustion air at engine full-load operating conditions.

5.3 Budgeting of Capital

Because the oxygen-enrichment system under consideration requires relatively large capital outlays, capital budgeting is used in the financial analysis. The method of capital budgeting is that followed by Ragland and Whipple (1989) and Cole et al. (1990), who made similar studies in evaluating the economics of an oxygen-enrichment system for industrial applications. In this analysis, three capital budgeting approaches were used: net present value (NPV), internal rate of return (IRR), and simple payback.

The NPV can be used to test the economic feasibility while pursuing any big capital outlay project. It is generally accepted that if the project NPV is positive, it is economically more desirable to pursue. On the other hand, if the project NPV is negative, the project investment will never be recovered at the discount rate, and so the project should not be undertaken. NPV can

TABLE 5.2 Capital Costs of Base Engine and Engine Supplied with 26% Oxygen-Enriched Air

Engine Parameters	Ambient Air	Oxygen-Enriched Air without Exhaust Recovery		Oxygen-Enriched Air with Exhaust Recovery	
Membrane material	-	CMS-3	CMS-7	CMS-3	CMS-7
Oxygen concentration, by vol. (%)	21	26	26	26	26
Gross power (bhp)	2500	3188	3188	3188	3188
Membrane work (bhp)	-	441	540	441	540
Exhaust recovery (bhp)	-	-	-	196	196
Net power (bhp)	2500	2747	2648	2943	2844
Engine cost (@300/bhp)	$750,000	$824,100	$794,400	$882,900	$853,200
Gain in engine capital	-	$74,100	$44,400	$132,900	$103,200
OEA equipment cost	-	$230,544	$233,829	$230,544	$233,829
Exhaust recovery system	-	-	-	$98,000	$98,000
Differential capital investment	-	$156,444	$189,429	$195,644	$228,629

also be used to rank several projects of the same type; if Project A's NPV is greater than Project B's NPV, then Project A is the more desirable alternative. The NPV of a project is found by summing the present values of the annual year-end cash flows over a project's lifetime less the initial outlay and is given by

$$NPV = \sum \frac{CF_i}{(1+k)^i} \tag{5.1}$$

where CF_i is cash flow at time i; k is interest rate (or discount rate); and i is the time period (usually years), equal to zero at time zero.

The IRR of a project is that discount rate that makes the NPV of a project equal to zero. If the IRR of a project is greater than the required rate of return (discount rate), then a project should be undertaken. The project with the highest IRR is obviously preferable in economic terms. The IRR can also be used to rank projects having similar NPVs.

The simple payback period of a project is the time required to pay the initial outlay from the expected cash inflow. Obviously, the project with shortest payback period is the most desirable one. However, the payback method ignores both the time value of money and any cash flows that occur after the payback period. But, when combined with such other capital budgeting methods as NPV and IRR, the simple-payback approach can be useful.

5.4 Cash Flow Analysis

The key component of the capital budgeting process is to estimate the annual cash flows for a project. To arrive at a net cash flow for a given year, several factors have to be taken into account, such as cash inflows, equipment depreciation, overhead, and salvage value. The cash inflows are the annual cost savings that would be realized by operating a locomotive diesel engine with oxygen-enriched intake air, compared to the cost of operating a locomotive diesel engine with ambient intake air.

Generally, equipment depreciation would be considered for big capital outlays. The equipment needed for the oxygen-enrichment system is assumed to fall in the seven-year accelerated cost recovery system (ACRS) class, which provides allowable depreciation as a function of the equipment age under current tax regulations. Since the ACRS operates on half-year increments, the depreciation is taken over eight years according to the schedule shown in Table 5.3. The actual money that is saved by depreciating an asset is the tax saving. With a corporate tax rate of 34%, the tax saving due to depreciation for a given year is computed. The lifetime of the membrane is assumed to be eight years. The replacement membranes are assumed to fall into a seven-year ACRS class, beginning when they are purchased. The average lifetime of auxiliary equipment (blower, vacuum pump etc.) was taken to be 15 years; thus, the project lifetime was assumed to be 15 years. Some miscellaneous factors that go into annual cash flows

are operation and maintenance (O&M) costs and end-of-project cash flows, such as salvage value or return of capital. The annual O&M costs were assumed to be 2% of initial capital equipment costs (excluding membrane cost). The load factor was assumed to be 80% (7,000 h/yr) at engine full load (notch 8). The energy cost was assumed to be $0.15/bhp-hr, and diesel fuel cost was assumed to be $0.6 per gallon. The assumptions about the economic parameters are summarized in Table 5.4. Finally, at the end of the project, the capital equipment had an estimated 10% salvage value. Thus, the net cash flow (NCF) for a period is calculated as follows:

NCF = cash inflow + depreciation tax savings - overhead - membrane replacement cost + salvage value - tax on salvage value (5.2)

The NCFs for each period were adjusted for annual inflation (assumed to be 5%) because the NPV of a project would be downward-biased if this was not taken into account.

TABLE 5.3 Allowable Tax Depreciation per ACRS

Year	Depreciation (%)
1	14
2	25
3	17
4	13
5	9
6	9
7	9
8	4

TABLE 5.4 Assumptions about Economic Parameters

Parameter	Value
Inflation rate	5%
Discount rate	15%
Corporate tax rate	34%
Maintenance costs	2% of initial hardware costs
Labor cost	2 h/wk @ $15/h
Equipment life	15 yr
OEA element's life	7 yr
Salvage value	10%
Load factor	80% (7000 h/yr)
Energy cost	$0.15/bhp-h
Diesel fuel cost	$0.6/gal

5.5 Results of Economic Analysis

The net cash savings for the first year were obtained for an engine supplied with ambient air (21% oxygen concentration) and an engine supplied with 26% oxygen-enriched air, using CMS-3 and CMS-7 membrane materials; results are shown in Table 5.5. First-year savings were computed from the increased energy production and increased fuel costs. The potential economic benefit of recovering exhaust energy from an engine supplied with oxygen-enriched combustion air is also shown, in terms of net cash savings per year. On the basis of net cash savings per year, the cash-flow analysis for both CMS membrane materials supplying 26% oxygen-enriched air to the engine operating at full load was performed, using three methods of capital budgeting; results are shown in Tables 5.6 and 5.7. Similarly, the cash-flow analysis was done for both membrane materials, including exhaust energy recovery from the engine; results are presented in Tables 5.8 and 5.9. The results of the economic analyses for all four cases are summarized in Table 5.10.

Between the two CMS materials (see Tables 5.6 and 5.7), the CMS-3 membrane has the shortest simple payback period (1.13 yr) and the highest IRR (95.8%). CMS-3 has the highest NPV and hence offers the greater savings over a 15-year period as compared to the CMS-7 membrane. Conversely, CMS-7 has the longest payback period because the net cash savings were low as a result of higher parasitic power requirements. Although the fuel consumption was the same for both the CMS-3 and CMS-7 membranes, the energy output was considerably lower with CMS-7 than with CMS-3. Thus, the first-year savings for CMS-7 are relatively low; a period of about 5.5 yr is required to recover the initial capital investment. The advantage of CMS-7 in terms of lower membrane cost was not reflected in lower capital cost because the auxiliary equipment costs were considerably higher (by $45,500) compared to those for the CMS-3 membrane. The difference in initial investment between the CMS-3 and CMS-7 membranes was little, but the net cash savings per year was relatively higher because of

TABLE 5.5 First-Year Net Cash Savings

Parameter	Ambient Air	Oxygen-Enriched Air without Exhaust Recovery		Oxygen-Enriched Air with Exhaust Recovery	
Membrane	-	CMS-3	CMS-7	CMS-3	CMS-7
Net power, bhp	2500	2747	2648	2943	2844
Load (factor of 90%) h/yr	7000	7000	7000	7000	7000
Energy, bhp-h	17500000	19229000	18536000	20601000	19908000
Energy cost (@$0.15/bhp-h)	$2,625,000	$2,884,350	$2,780,400	$3,090,150	$2,986,200
Energy savings/yr	-	$259,350	$155,400	$465,150	$361,200
Fuel consumption, lb/h	862.2	1063.92	1063.92	1063.92	1063.92
Total fuel consumption, gal/yr	862200	1063920	1063920	1063920	1063920
Fuel cost (@$0.6/gal)	$517,320	$638,352	$638,352	$638,352	$638,352
Increase in fuel cost/yr	-	$121,032	$121,032	$121,032	$121,032
Net cash savings/yr	-	$138,318	$34,368	$344,118	$240,168

TABLE 5.6 Cash-Flow Analysis for CMS-3 Membrane with 26% Oxygen

Year	Initial Investment	Annual Cost Savings	Annual Deprec.	Annual Tax Savings	Annual Labor	Annual Maintenance	OEA Replacement Cost	Salvage Value	Tax on Salvage	Net Cash Flow	Inflation-Adjusted NCF	NPV
Year 0	156444									-156444	-156444	-156444
Year 1		138318	21902	7447	1560	2540				141665	148748	129346
Year 2		138318	39111	13298	1560	2540				147516	154892	117120
Year 3		138318	26595	9042	1560	2540				143260	150423	98906
Year 4		138318	20338	6915	1560	2540				141133	148189	84728
Year 5		138318	14080	4787	1560	2540				139005	145955	72566
Year 6		138318	14080	4787	1560	2540				139005	145955	63101
Year 7		138318	14080	4787	1560	2540				139005	145955	54870
Year 8		138318	17198	5847	1560	2540	78144			61921	65017	21254
Year 9		138318	19536	6642	1560	2540				140860	147903	42043
Year 10		138318	13284	4517	1560	2540				138735	145671	36008
Year 11		138318	10159	3454	1560	2540				137672	144556	31071
Year 12		138318	7033	2391	1560	2540				136609	143440	26810
Year 13		138318	7033	2391	1560	2540				136609	143440	23313
Year 14		138318	7033	2391	1560	2540				136609	143440	20272
Year 15		138318	3126	1063	1560	2540		12700	4318	143663	150846	18538
Total												683502

TABLE 5.7 Cash-Flow Analysis for CMS-7 Membrane with 26% Oxygen

Year	Initial Investment	Annual Cost Savings	Annual Deprec.	Annual Tax Savings	Annual Labor	Annual Maintenance	OEA Replacement Cost	Salvage Value	Tax on Salvage	Net Cash Flow	Inflation-Adjusted NCF	NPV
Year 0	189429									-189429	-189429	-189429
Year 1		34368	26520	9017	1560	3450				38375	40294	35038
Year 2		34368	47357	16101	1560	3450				45459	47732	36093
Year 3		34368	32203	10949	1560	3450				40307	42322	27828
Year 4		34368	24626	8373	1560	3450				37731	39617	22651
Year 5		34368	17049	5797	1560	3450				35155	36912	18352
Year 6		34368	17049	5797	1560	3450				35155	36912	15958
Year 7		34368	17049	5797	1560	3450				35155	36912	13877
Year 8		34368	11333	3853	1560	3450	26829			6382	6701	2191
Year 9		34368	6707	2280	1560	3450				31638	33220	9443
Year 10		34368	4561	1551	1560	3450				30909	32454	8022
Year 11		34368	3488	1186	1560	3450				30544	32071	6893
Year 12		34368	2415	821	1560	3450				30179	31688	5923
Year 13		34368	2415	821	1560	3450				30179	31688	5150
Year 14		34368	2415	821	1560	3450				30179	31688	4478
Year 15		34368	1073	365	1560	3450		17250	5865	41108	43163	5305
Total												27773

differences in energy output. This indicates that a membrane with lower parasitic power requirements is economically preferable compared to a membrane with low cost (surface area) to deliver equal amounts of air flow at any desired oxygen concentration. Therefore, on the basis of the present economic study, the CMS-3 membrane appears to be the most economically attractive option to obtain the benefits from oxygen-enrichment technology in a locomotive diesel engine.

It was evident from the engine simulation results (see Section 4.8) that exhaust energy recovery can realize the full potential of oxygen-enrichment technology for improving the performance of locomotive diesel engines. In order to explore its economic advantage, the cash-flow analyses were done by considering the energy benefits and appropriate capital investments. In this case also, two different membranes were considered for the analysis (see Tables 5.8 and

TABLE 5.8 Cash-Flow Analysis for CMS-3 Membrane with 26% Oxygen and with Exhaust Energy Recovery

Year	Initial Investment	Annual Cost Savings	Annual Deprec.	Annual Tax Savings	Annual Labor	Annual Maintenance	OEA Replacement Cost	Salvage Value	Tax on Salvage	Net Cash Flow	Inflation-Adjusted NCF	NPV
Year 0	195644									-195644	-195644	-195644
Year 1		344118	27390	9313	1560	2540				349331	366797	318954
Year 2		344118	48911	16630	1560	2540				356648	374480	283161
Year 3		344118	33259	11308	1560	2540				351326	368893	242553
Year 4		344118	25434	8647	1560	2540				348665	366099	209318
Year 5		344118	17608	5987	1560	2540				346005	363305	180627
Year 6		344118	17608	5987	1560	2540				346005	363305	157067
Year 7		344118	17608	5987	1560	2540				346005	363305	136580
Year 8		344118	18766	6380	1560	2540	78144			268254	281667	92077
Year 9		344118	19536	6642	1560	2540				346660	363993	103470
Year 10		344118	13284	4517	1560	2540				344535	361761	89422
Year 11		344118	10159	3454	1560	2540				343472	360646	77518
Year 12		344118	7033	2391	1560	2540				342409	359530	67199
Year 13		344118	7033	2391	1560	2540				342409	359530	58434
Year 14		344118	7033	2391	1560	2540				342409	359530	50812
Year 15		344118	3126	1063	1560	2540		12700	4318	349463	366936	45094
Total												1916641

TABLE 5.9 Cash-Flow Analysis for CMS-7 Membrane with 26% Oxygen and with Exhaust Energy Recovery

Year	Initial Investment	Annual Cost Savings	Annual Deprec.	Annual Tax Savings	Annual Labor	Annual Maintenance	OEA Replacement Cost	Salvage Value	Tax on Salvage	Net Cash Flow	Inflation-Adjusted NCF	NPV
Year 0	228629									-228629	-228629	-228629
Year 1		240168	32008	10883	1560	3450				246041	258343	224646
Year 2		240168	57157	19433	1560	3450				254591	267321	202133
Year 3		240168	38867	13215	1560	3450				248373	260791	171475
Year 4		240168	29722	10105	1560	3450				245263	257527	147242
Year 5		240168	20577	6996	1560	3450				242154	254262	126413
Year 6		240168	20577	6996	1560	3450				242154	254262	109924
Year 7		240168	20577	6996	1560	3450				242154	254262	95586
Year 8		240168	12901	4386	1560	3450	26829			212715	223351	73014
Year 9		240168	6707	2280	1560	3450				237438	249310	70870
Year 10		240168	4561	1551	1560	3450				236709	248544	61436
Year 11		240168	3488	1186	1560	3450				236344	248161	53341
Year 12		240168	2415	821	1560	3450				235979	247778	46311
Year 13		240168	2415	821	1560	3450				235979	247778	40271
Year 14		240168	2415	821	1560	3450				235979	247778	35018
Year 15		240168	1073	365	1560	3450		17250	5865	246908	259253	31861
Total												1260912

5.9). When a portion of the exhaust energy is recovered while the engine is supplied with 26% oxygen-enriched combustion air, the NPV and IRR are higher, and the simple payback period is lower, for both membranes (as compared to the cases without exhaust recovery). In the case of the CMS-3 membrane, the NPV increased from $683,502 to $1,916,641; the IRR increased from 95.82% to 188.41%; and the simple payback period was lowered from 1.13 yr to 0.57 yr (see Table 5.10). The greatest economic advantages of exhaust energy recovery can be observed in the case of the CMS-7 membrane. With the CMS-7 membrane, the capital investment could be recovered within 0.95 yr, compared to 5.5 yr if part of the exhaust energy was recovered. Also, the NPV increased from $27,773 to $1,260,912, and IRR increased from 18.2% to 113.9%.

TABLE 5.10 Summary of Economic Analysis

	Budget Criteria			
Case	Capital Cost ($)	NPV ($)	IRR (%)	Simple Payback (yr)
26% oxygen-enriched air, CMS-3 membrane	156,444	683,502	95.82	1.13
26% oxygen-enriched air, CMS-7 membrane	189,429	27,773	18.27	5.51
26% oxygen-enriched air, CMS-3 membrane with exhaust energy recovery	195,644	1,916,641	188.41	0.57
26% oxygen-enriched air, CMS-3 membrane with exhaust energy recovery	228,629	1,260,912	113.95	0.95

These data underline the importance of recovering exhaust energy to obtain the greatest benefits with regard to both performance and economics. It was apparent that any attempt to increase the energy output had a significant economic benefit. The capital investment needed to recover the exhaust energy represents an increase of only $98,000, but the economic benefits are very significant in terms of higher IRR and NPV, and lower simple payback periods, using either the CMS-3 or CMS-7 membrane. The increase in capital investment needed to recover a part of the exhaust energy is highly justifiable, because the increase in cash savings is very significant as a result of the higher energy output.

The present study is focused only on two membrane materials because of the limited availability of technical and economic data. To refine and broaden the economic study, knowledge of the costs of various membranes and auxiliary equipment to supply different oxygen-enrichment levels is required. However, the objective of the present study is only to illustrate economic feasibility for a given membrane and to supply a specified oxygen-enrichment level (26% by volume) for a locomotive diesel engine.

On the basis of the present economic analysis, a locomotive engine operating with 26% oxygen-enriched combustion air, supplied by a CMS-3 membrane, appears to be economically attractive with or without exhaust energy recovery. This is clearly demonstrated by the economic performance indicators, such as low simple payback period (0.57 yr and 1.13 yr with and without exhaust recovery, respectively) and high NPV and IRR. Membranes with higher parasitic power requirements, such as CMS-7, need a part of the exhaust energy to be recovered to justify the capital investment and to improve the economic advantage. The study also shows that membrane parasitic power requirements have the greatest influence on the performance and economic benefits of oxygen-enrichment technology. Membrane size or cost is considered to have relatively lesser impact on the economic benefits as compared to the membrane power requirements.

6 Summary and Conclusions

A thermodynamic diesel engine simulation and a simplified model of the air separator membrane were used to study the effects of different intake air oxygen-enrichment levels on the performance and NO emissions of a locomotive diesel engine.

The following conclusions can be drawn from this investigation:

1. At notch 8 (full load), when the intake air oxygen concentration was increased from 21 to 35% (by volume) while a constant oxygen-to-fuel ratio was maintained in the combustion mixture, the cylinder brake output and brake mean effective pressure increased by up to 90%, and brake-specific fuel consumption decreased by as much as 15%. However, the corresponding peak cylinder pressure increased by up to 35%.

2. Retarding the fuel injection timing when oxygen-enriched intake air was used had a beneficial effect with respect to peak cylinder pressure, without imposing severe penalties on power and fuel consumption. For intake air, oxygen levels varied between 23 and 30% (by volume), and with retarded fuel injection timing (up to 12 degrees crank angle), the peak cylinder pressure was decreased by up to 22%, with only a marginal penalty (on the order of 4%) in power and fuel consumption.

3. NO emissions computed on the basis of adiabatic flame temperature increased by up to four times when the intake air oxygen concentration was increased from 21 to 35%. Although retarding fuel injection timing can somewhat reduce NO emissions associated with oxygen-enriched combustion, another post-treatment device is needed to comply with the NO emission standards.

4. To provide intake air with 23 to 30% oxygen content (by volume) for a 12-cylinder locomotive diesel engine operating at full load would require between 150 and 650 hp to drive the auxiliary equipment; the corresponding membrane area was estimated to occupy between 10 and 30 cubic feet, depending on the desired level of oxygen enrichment. However, an extensive optimization of several membrane parameters is necessary to refine the estimates of membrane power and size for a desired enrichment level and air flow.

5. On the basis of a preliminary membrane design and its power requirements, the net brake power improvement obtained from an engine operating with oxygen-enriched air (from 23 to 30% by volume) supplied by an air separation membrane was only between 4 and 15%. For the same inlet conditions, the cylinder brake output (without the parasitic membrane work) improved substantially, between 10 and 46%. Any reduction in membrane power requirements would have an obvious direct impact on net power improvement.

6. When peak cylinder pressure is controlled by retarding fuel injection timing, oxygen enrichment has the potential to provide greater improvements in brake power than those obtained by other methods, such as high-boost turbocharging. For instance, a 4% increase in peak cylinder pressure can result in a 13% increase in net engine power with oxygen enrichment but only a 4% increase with high-boost turbocharging. In addition, recovering part of the increased exhaust energy through a bottoming cycle can make the oxygen-enriched concept far more attractive than other methods of boosting power at a constant peak cylinder pressure.

7. Since the required modifications to the intake system are not complex, a membrane device can be readily retrofitted to in-use locomotives. Oxygen-enrichment technology promises to provide a significant power boost on sudden demand or continuously, alleviate concerns about certain exhaust emissions (visible smoke, particulates, and unburned hydrocarbons), and enable the use of lower-grade fuels.

8. The application of oxygen-enrichment technology for locomotive diesel engines is economically feasible and can provide a high internal rate of return on the investment. However, the economic benefits are strongly dependent on the membrane parasitic power requirements and energy recovered from the exhaust. Membrane (size) cost and auxiliary equipment cost affect the economics less significantly. The study emphasizes the need to optimize the oxygen-enrichment system for maximum economic benefits.

9. On the basis of economic analysis, a locomotive diesel engine operating with 26% oxygen-enriched combustion air, supplied by a CMS-3 membrane, has a short simple payback period of 1.13 yr and an IRR of 95.8%. When a portion of the exhaust energy is recovered, the simple payback period is reduced to 0.57 yr and IRR is increased to 188.4%.

10. Between the two membrane materials considered for supplying 26% oxygen-enriched combustion air for a 12-cylinder locomotive diesel engine, CMS-7 (which has higher parasitic power requirements) has a longer payback period (5.5 yr) and gives a lower IRR (18.2%) than does the CMS-3 membrane. In order to get economic benefits while using such membranes (such as CMS-7) with high parasitic power requirements, it is necessary to recover part of the exhaust energy. When a part of the exhaust energy is recovered while the CMS-7 membrane is supplying 26% oxygen-enriched combustion air, the simple payback period is reduced from 5.5 yr to 0.95 yr, NPV is increased from $27,773 to $1,260,912, and IRR is increased from 18.2 to 113.9%, compared to the case without exhaust recovery.

7 References

Anand, J.N., S.E. Bales, D.C. Feay, and T.O. Jeanes, 1989, "Tetrabromo Bisphenol Based Polycarbonate Membranes and Method of Using," U.S. Patent 4,840,646.

Annand, J.D., 1963, "Heat Transfer in the Cylinders of Reciprocating Internal Combustion Engines," Proc. Inst. of Mech. Eng., Vol. 177, No. 36.

Annand, J.D., and T.H. Ma, 1971, "Instantaneous Heat Transfer Rates to the Cylinder Head Surface of a Small Compression-Ignition Engine" (Second Paper), Proc. Inst. of Mech. Eng., Vol. 185, No. 72.

Assanis, D.N., 1985, "A Computer Simulation of the Turbocharged Turbocompound Diesel Engine System for Studies of Low Heat Rejection Engine Performance," Ph.D. Thesis, Massachusetts Institute of Technology.

Assanis, D.N., and J.B. Heywood, 1986, "Development and Use of a Computer Simulation of the Turbocompound Diesel Engine System for Engine Performance and Component Heat Transfer Studies," SAE Paper 860329.

Assanis, D.N., R.R. Sekar, D. Baker, C.T. Ciambekos, R.L. Cole, and T.J. Marciniak, 1990, "Simulation Studies of Diesel Engine Performance with Oxygen Enriched Air and Water Emulsified Fuels," ASME Paper 90-ICE-17.

Assanis, D.N., 1991, "A Computer Simulation of Diesel Engine Performance with Oxygen Enriched Air," Technical Report, University of Illinois at Urbana-Champaign, UILU-91-4007.

Assanis, D.N., E. Karvounis, R.R. Sekar, and W.W. Marr, 1993, "Heat Release Analysis of Oxygen-Enriched Diesel Combustion," ASME Journal of Engineering for Gas Turbines and Power, Vol. 115, pp. 761-768.

Baker, R.H., E.L. Cussler, W. Eykamp, W.J. Koros, R.L. Riley, and H. Strathmann, 1990, "Membrane Separation Systems: A Research Needs Assessment Final Report," U.S. Department of Energy, Vol. 2, DOE/ER/30133-H1.

Brandup, J., and E.H. Immergut, 1975, *Polymer Handbook* (Second Edition), John Wiley and Sons.

Chern, R.T., W.J. Koros, and P.S. Fedklw, 1985, "Simulation of a Hollow-Fiber Gas Separator: The Effects of Process and Design Variables," Ind. Eng. Chem. Process Des. Dev., Vol. 24, pp. 1015-1022.

Cole, R.L., R.R. Sekar, F. Stodolsky, and T. Marciniak, 1990, "Technical and Economic Evaluation of Diesel Engine with Oxygen Enrichment and Water Injection," ASME Energy-Sources Technology Conference and Exhibition, Paper No. 90-ICE-1.

Dent, J.C., and S.J. Suliaman, 1977, "Convective and Radiative Heat Transfer in a High Swirl Direct Injection Diesel Engine," SAE Paper 770407.

Ebersole, G.D., P.S. Myers, and O.A. Uyehara, 1963, "The Radiative and Convective Components of Diesel Engine Heat Transfer," SAE Paper 701C.

Fleming, G., 1996, Cochrane Compressor Company, Melrose Park, Illinois, personal communication.

Flynn, P., M. Mizusawa, O.A. Uyehara, and P.S. Myers, 1972, "An Experimental Determination of the Instantaneous Potential Radiant Heat Transfer within an Operating Diesel Engine," SAE Paper 720022.

Ghojel, J., J.C. Hillard, and J.A. Levendis, 1983, "Effect of Oxygen-Enrichment on the Performance and Emissions of IDI Diesel Engines," SAE Paper 830245.

Gollan, A.Z., and M.H. Kleper, 1985, "Research into an Asymmetric Membrane Hollow Fiber Device for Oxygen-Enriched Air Production," U.S. Department of Energy, DOE/ID-12429-1.

Heywood, J.B., 1988, *Internal Combustion Engine Fundamentals*, McGraw-Hill Book Co., New York, N.Y.

Igura, S., T. Kadota, and H. Hirozasu, "Spontaneous Ignition Delay of Fuel Sprays in High Pressure Gaseous Environment," Japan Society of Mechanical Engineers, Vol. 41, No. 345, p. 1559.

Iida, N., and G.T. Sato, 1988, "Temperature and Mixing Effects on NO_x and Particulates," SAE Paper 880424.

Kamel, M., and N. Watson, 1979, "Heat Transfer in the Indirect Injection Diesel Engine," SAE Paper 790826.

Koros, W.J., and R.T. Chern, 1987, *Handbook of Separation Process Technology*, John Wiley and Sons.

Kunitomo, T., K. Matsuoka, and T. Oguri, 1975, "Prediction of Radiative Heat Flux in a Diesel Engine," SAE Paper 750786.

Lavoie, G. A., J. B. Heywood, and J. C. Keck, 1970, "Experimental and Theoretical Investigation of Nitric Oxide Formation in Internal Combustion Engines," Combustion Science and Technology, Vol. 1, pp. 313-326.

Lyn, W.T., 1962, "Study of Burning Rate and Nature of Combustion in Diesel Engine," IX Symposium (International) on Combustion, The Combustion Institute, Proceedings, pp. 1069-1082.

Mansouri, S.H., J.B. Heywood, and K. Radhakrishnan, 1982, "Divided-Chamber Diesel Engines, Part 1: A Cycle-simulation which Predicts Performance and Emissions," SAE Paper 820273.

Markworth, V.O., S.K. Widener, A.C. Matheaus, and R.L. Mason, 1993, "Locomotive Improvement Program - Twelfth Research Phase Final Report," Southwest Research Institute Report No. 03-4171/AAR Report No. R-841.

Martin, M.K., and J.B. Heywood, 1977, "Approximate Relationships for the Thermodynamic Properties of Hydrocarbon-Air Combustion Products," Combustion Science and Technology, Vol. 15, pp. 1-10.

Marr, W.W., R.R. Sekar, R.L. Cole, T.J. Marciniak, and D.E. Longman, 1993, "Oxygen-Enriched Diesel Engine Experiments with a Low-Grade Fuel," SAE Paper 932805.

Millington, B.W., and E.R. Hartles, 1968, "Frictional Losses in Diesel Engines," SAE Paper 680590.

Morel, T., R. Keribar, and P.N. Blumberg, 1985, "Cyclic Thermal Phenomena in Engine Combustion Chamber Surfaces," SAE Paper 850360.

Ng, H.K., V.J. Novick, and R.R. Sekar, 1995, "Using Monatomic Nitrogen Induced by a Pulsed Arc to Remove Nitrogen Oxides From a Gas Stream," ASME Fall Technical Conference, Vol. 1, pp. 73-80.

Nemser, S.M., and I.C. Roman, 1991, "Perfluorodioxole Membranes," U.S. Patent 5,051,114.

Nemser, S.M, 1996, Compact Membrane Systems, Inc., Wilmington, Del., personal communication.

Oguri, T., and I. Shigewo, 1972, "Radiant Heat Transfer in Diesel Engines," SAE Paper 720023.

Pan, C.Y., 1986, "Gas Separation by High-Flux, Asymmetric Hollow-Fiber Membrane," AIChE Journal, Vol. 32, No. 12, pp. 2020-2027.

Plee, S.L., T. Ahmad, and J.P. Myers, 1982, "Diesel NO_x Emissions - A Simple Correlation Technique for Intake Air Effects," Nineteenth Symposium (International) on Combustion, The Combustion Institute, pp. 1495-1502.

Ragland, K.W., and J.G. Whipple, 1989, "Test and Evaluation of Polymeric Membranes for Oxygen-Enrichment of Air," U.S. Department of Energy, DOE/ID-12710-1.

Sawyer, R.F., N.P. Cernansky, and A.K. Oppenheim, 1973, "Factors Controlling Pollutant Emissions from Gas Turbine Engines," Atmospheric Pollution by Aircraft Engines, AGARD CP-125, Paper No. 22.

Sekar, R.R., W.W. Marr, R.L. Cole, T.J. Marciniak, and J.E. Schaus, 1990, "Diesel Engine Experiments with Oxygen Enrichment, Water Addition, and Lower-Grade Fuel," Twenty-Fifth Intersociety Energy Conversion Engineering Conference, Reno, Nev.

Sekar, R.R., W.W. Marr, D.N. Assanis, R.L. Cole, T.J. Marciniak, and J.E. Schaus, 1991a, "Oxygen-Enriched Diesel Engine Performance: A Comparison of Analytical and Experimental Results," ASME Journal of Engineering for Gas Turbines and Power, Vol. 113, pp. 365-369.

Sekar, R.R., W.W. Marr, R.L. Cole, and T.J. Marciniak, 1991b, "Effects of Oxygen Enrichment and Fuel Emulsification on Diesel Engine Performance and Emissions," ASME Meeting on Fuels, Controls and Aftertreatment for Low-Emissions Engines, Internal Combustion Engines Division, Vol. 15, pp. 21-28.

Shampine, L.F., and M.K. Gordon, 1974, *Computer Solution of Ordinary Differential Equations: The Initial Value Problem*, Freeman.

Sitkei, G., 1974, *Heat Transfer and Thermal Loading in Internal Combustion Engines*, Akademiai Kiade, Budapest.

Spadaccini, L.J., and J.A. TeVelde, 1980, "Autoignition Characteristics of Aircraft-Type Fuels," United Technologies Research Center, NASA Report CR-159886.

Streit, E., and G. Borman, 1971, "Mathematical Simulation of a Large Turbocharged Two-Stroke Diesel Engine," SAE Paper 710176.

Stringer, F.W., A.E. Clarke, and J.S. Clarke, 1970, "The Spontaneous Ignition of Hydrocarbon Fuels in a Flowing System," Proc. Inst. of Mech. Eng., Automobile Division.

Svehla, R.A., and B.J. McBride, 1973, "FORTRAN IV Computer Program Calculations of Thermodynamic and Transport Properties of Complex Chemical Systems," NASA Technical Note, NASA TN d-7056.

Tennekes, M., and J.L. Lumley, 1972, A *First Course in Turbulence,* M.I.T. Press, Cambridge, Mass.

Watson, N., A.D. Pilley, and M. Marzouk, 1980, "A Combustion Correlation for Diesel Engine Simulation," SAE Paper 800029.

Whitehouse, N.D., 1971, "Heat Transfer in a Quiescent Chamber Diesel Engine," Proc. Inst. Mech. Eng., Vol. 185, No. 72.

Winston Ho, W.S., and K.K. Sirkar, 1992, *Membrane Handbook*, Chapman & Hall, New York.

Woschni, G., 1977, "A Universally Applicable Equation for the Instantaneous Heat Transfer Coefficient in the Internal Combustion Engines," SAE Paper 670931.

Appendix:

Scope of Work for Phase II

A.1 Purpose

The purpose of the CRADA, Phase II, is to demonstrate the use of oxygen-enrichment technology for locomotive diesel engines. The key technical issues to be addressed in the project include (1) optimization of the level of oxygen enrichment in the intake air, both analytical and experimental; (2) the development, design, and fabrication of an air separation membrane; and (3) solutions to control NO_x emissions, such as retarded fuel injection timing and use of monatomic nitrogen induced by a pulsed arc. If proven feasible, oxygen-enriched combustion using an air separation membrane (with solutions to control NO_x emissions) will be demonstrated in a locomotive diesel engine.

A.2 Scope of Work

The work for this Phase II CRADA is estimated to take three years to complete. Work in the first year will concentrate on two-cylinder, diesel engine tests with bottled oxygen to obtain design parameters for the air separation membrane device and NO_x control system. Work in the second year will concentrate on the design, development, fabrication, and procurement of necessary hardware to be used in a two-cylinder engine demonstration of the oxygen-enrichment and NO_x control systems. Year-3 work involves the testing of the prototype system on a two-cylinder locomotive diesel engine and design specifications of a prototype system for an operating locomotive. If it is agreeable to all parties, and subject to the availability of additional funding, full-scale demonstration tests with prototype systems will be conducted on a locomotive.

Work scope tasks are as follows:

Task 1: Laboratory Engine Tests with Bottled Oxygen

ANL will guide the two-cylinder diesel engine tests to obtain performance and emissions data at three different levels of oxygen-enriched intake air by using bottled oxygen. ANL will support to setup the air handling and oxygen-supply systems to provide increasing oxygen concentrations of up to 30% by volume in the engine intake air. Both ANL and AAR will equally share the cost of conducting the laboratory engine tests at either AutoResearch Laboratories, Inc., or at the Southwest Research Institute. ANL will plan and execute the tests and analyze the data. Only a bare minimum amount of testing will be conducted with bottled oxygen, primarily to define the parameters of the specific engine. Depending on the NO_x emissions levels, fuel injection timing will be retarded along with the oxygen-enriched intake air. Test results will be analyzed and the emissions data will be converted by analytical techniques to locomotive duty cycle emissions (in grams per mile) for a typical route.

AAR will locate a suitable test facility for two-cylinder experiments. The budget estimates for conducting the test matrix as suggested by ANL will be obtained from various testing laboratories. AAR will support the total cost to conduct the two-cylinder engine test matrix. Along with ANL, AAR will take part in reviewing the two-cylinder test results.
(months 1-5)

Task 2: Analysis of Engine Test Data

ANL will review the test results from Task 1 and finalize the optimal oxygen-enrichment level, engine air and fuel flow rates, and fuel injection timing for the test engine. Engine analytical models to predict performance using oxygen-enriched intake air will be calibrated with the experimental data obtained from Task 1. ANL will examine various physical and operating characteristics of a typical air separation membrane for application in locomotive engines. A suitable working (analytical) model will be developed to predict the performance of an air separation module. Several design factors will be studied to optimize both the membrane module size and parasitic power requirements. A bench test facility will be developed to test and evaluate the module size and power requirements of prototype membranes. The test results will be used to calibrate the membrane model. Calibrated membrane and engine models will be used to obtain *net benefits* in performance from locomotive diesel engines.

AAR will participate in the review of test results obtained from Task 1.
(months 6-8)

Task 3: Design of Membrane and NO_x Control Devices

ANL will design a prototype air separation membrane module and other auxiliary equipment for a demonstration test on a two-cylinder locomotive diesel engine. Economic tradeoffs among membrane costs, auxiliary equipment costs, input power requirements (to maintain required pressure/vacuum), and system compactness will be evaluated. ANL will pursue the NO_x control technologies. The effectiveness of monatomic nitrogen induced by a pulsed electric arc in reducing NO_x will be tested in the ANL laboratory by using simulated diesel engine exhaust. The requirements of a monatomic nitrogen generator with regard to purity of nitrogen, nitrogen-rich air flow, power for generating plasma arc, and a compact device (like a sparking device) to install in the exhaust will be evaluated. If results are encouraging, a prototype monatomic sparking device will be designed for NO_x after-treatment. If a NO_x problem still persists, then such other technologies as variable intake air composition and lean NO_x catalysts will be evaluated.

AAR will review the design details and obtain concurrence from the railroad engineering department.
(months 9-15)

Task 4: Laboratory Evaluation of Engine-System Components

On the basis of the design drawings produced in Task 3, ANL will procure a prototype air separation membrane, NO_x control device, and other necessary auxiliary parts for a demonstration test in a two-cylinder engine. Each of the prototype components will be tested by ANL before installation in order to ensure component performance as well as fitness for evaluation in an actual engine. All components will be returned to the Contractor at the end of the project. ANL will provide for all the costs of the oxygen-enrichment system.

AAR will assist in assembling all the prototype components. Arrangements will be made for installation of these components in a specific engine platform.
(months 16-22)

Task 5: Two-Cylinder Engine Demonstration

ANL, with input from AAR, will develop a test plan for two-cylinder engine demonstration tests with the prototype oxygen-enrichment and NO_x control systems. ANL will guide the experiments and analyze the results.

AAR will cover the total costs of the two-cylinder demonstration tests with the prototype (oxygen-enrichment and NO_x) systems. AAR will take part in reviewing test results. Recommendations/feedback from the AAR's member railroads will be provided with regard to installation of an oxygen-enrichment system on a locomotive.
(months 23-29)

Task 6: Design of Oxygen-Enrichment System for a Full-Size Locomotive

ANL will design the specifications of oxygen-enrichment and NO_x control systems for a 12-cylinder (EMD-710G) locomotive diesel engine. ANL, with input from AAR, will develop a test plan for a full-scale locomotive demonstration. Consistent with the available funds and interest level from AAR, a prototype (oxygen-enrichment and NO_x) system will be assembled for full-scale demonstration tests on a 12-cylinder locomotive engine. Necessary guidance and technical support will be provided for the demonstration tests.

AAR will assist in designing the prototype system for a locomotive fitted with a 12-cylinder engine. Consistent with the available funds and interest level from the member railroads, AAR will arrange and support 50% of the total costs of the full-scale demonstration tests in a locomotive. As a trade association of railroad companies, it is anticipated that one or more specific member companies will play an active role in this demonstration task.
(months 30-34)

Task 7: Final Report

ANL, with input from AAR, will prepare and submit a final report for the project. AAR will provide necessary information to the ANL for preparation of the final report of the project. The final report will be made available to the member railroads.
(months 35-36)